Title

Restoring retinal polyunsaturated fatty acid balance and retina function by targeting ceramide in AdipoR1-deficient mice.

Journal

Journal of Biological Chemistry, 300(5)

Authors

Lewandowski, Dominik

Gao, Fangyuan

Imanishi, Sanae

et al.

Publication Date

2024-05-01

DOI

10.1016/j.jbc.2024.107291

Peer reviewed

JBC RESEARCH ARTICLE

Restoring retinal polyunsaturated fatty acid balance and retina function by targeting ceramide in *AdipoR1*-deficient mice

Received for publication, February 23, 2024, and in revised form, March 30, 2024 Published, Papers in Press, April 16, 2024,
https://doi.org/10.1016/j.jbc.2024.107291

Dominik Lewandowski[1,*,‡], Fangyuan Gao[1,‡], Sanae Imanishi[2,3], Aleksander Tworak[1], Marco Bassetto[4], Zhiqian Dong[1], Antonio F. M. Pinto[5], Marcin Tabaka[6,7], Philip D. Kiser[1,4,8,9], Yoshikazu Imanishi[2,3], Dorota Skowronska-Krawczyk[1,4], and Krzysztof Palczewski[1,4,10,*]

From the [1]Gavin Herbert Eye Institute-Center for Translational Vision Research, Department of Ophthalmology, University of California, Irvine, California, USA; [2]Department of Ophthalmology, and [3]Stark Neurosciences Research Institute, Indiana University School of Medicine, Indianapolis, Indiana, USA; [4]Department of Physiology and Biophysics, University of California, Irvine, California, USA; [5]Clayton Foundation Laboratories for Peptide Biology, Salk Institute for Biological Studies, La Jolla, California, USA; [6]International Centre for Translational Eye Research, Warsaw, Poland; [7]Institute of Physical Chemistry, Polish Academy of Sciences, Warsaw, Poland; [8]Department of Clinical Pharmacy Practice, University of California, Irvine, California, USA; [9]Research Service, Veterans Affairs Long Beach Healthcare System, Long Beach, California, USA; [10]Department of Chemistry, and Department of Molecular Biology and Biochemistry, University of California, Irvine, California, USA

Reviewed by members of the JBC Editorial Board. Edited by George M. Carman

Mutations in the adiponectin receptor 1 gene (*AdipoR1*) lead to retinitis pigmentosa and are associated with age-related macular degeneration. This study explores the effects of AdipoR1 gene deficiency in mice, revealing a striking decline in ω3 polyunsaturated fatty acids (PUFA), an increase in ω6 fatty acids, and elevated ceramides in the retina. The AdipoR1 deficiency impairs peroxisome proliferator-activated receptor α signaling, which is crucial for FA metabolism, particularly affecting proteins associated with FA transport and oxidation in the retina and retinal pigmented epithelium. Our lipidomic and proteomic analyses indicate changes that could affect membrane composition and viscosity through altered ω3 PUFA transport and synthesis, suggesting a potential influence of AdipoR1 on these properties. Furthermore, we noted a reduction in the Bardet-Biedl syndrome proteins, which are crucial for forming and maintaining photoreceptor outer segments that are PUFA-enriched ciliary structures. Diminution in Bardet-Biedl syndrome-proteins content combined with our electron microscopic observations raises the possibility that AdipoR1 deficiency might impair ciliary function. Treatment with inhibitors of ceramide synthesis led to substantial elevation of ω3 LC-PUFAs, alleviating photoreceptor degeneration and improving retinal function. These results serve as the proof of concept for a ceramide-targeted strategy to treat retinopathies linked to PUFA deficiency, including age-related macular degeneration.

Recent technical advances have enabled studying the contribution of lipids as essential molecular moieties for structure, function, and signaling. Polyunsaturated fatty acids (PUFAs), notably long-chain (LC, 18–24 carbons) and very-long-chain (VLC, >24 carbons) omega-3 (ω3) PUFAs, are indispensable for the development and function of the retina, a light-sensitive tissue located in the posterior segment of the eye. PUFAs are essential components of photoreceptor outer segments (OSs) and disks where they play crucial structural and functional roles. They help maintain membrane fluidity and interact with rhodopsin to facilitate phototransduction (1). Furthermore, ω3 PUFAs serve as essential precursors for molecules that exhibit neuroprotective properties in the retina, including eicosanoids, docosanoids, elovanoids, neuroprotectins, and other molecules (2–4). Alterations in PUFA composition have been associated with several retinal diseases, including retinitis pigmentosa, age-related macular degeneration (AMD), and Stargardt macular dystrophy type 3, all of which can culminate in vision loss (5). While an imbalance in the ratios of ω3 to ω6 PUFAs in the retina has been linked to chronic inflammation—a precursor to many retinal diseases—the mechanisms that regulate PUFA content and maintain the balance between ω3 and ω6 PUFAs are not yet fully elucidated (6).

Adiponectin receptors are primarily represented by two isoforms, AdipoR1 and AdipoR2. Structurally, they resemble G-protein coupled receptors with their seven transmembrane domains. However, unlike typical G-protein coupled receptors, their topology is inverted, with an intracellular N terminus and an extracellular C terminus (7). These receptors regulate glucose and lipid metabolism and have intrinsic ceramidase activity (7–9). AdipoR1 and AdipoR2 demonstrate similar substrate specificity towards ceramide species, including C6, C18, and C24 (7). Importantly, mutations in the *ADIPOR1* gene have been identified as causal factors for nonsyndromic and syndromic retinitis pigmentosa in humans. Additionally,

‡ These authors contributed equally to this work.
* For correspondence: Krzysztof Palczewski, kpalczew@uci.edu; Dominik Lewandowski, lewandod@hs.uci.edu.

an association has been established between *ADIPOR1* gene mutation and advanced AMD within the Finnish population (10–12).

Within the retina, ADIPOR1 protein is distributed throughout, yet its most significant concentration is observed at the junction between the retinal pigmented epithelium (RPE) apical microvilli and the distal ends of the photoreceptor OSs, as evidenced by immunostaining. Nonetheless, Western blot analysis revealed a greater abundance of ADIPOR1 in the RPE than the neural retina (13).

Previously, we demonstrated that the absence of the *AdipoR1* gene in mice leads to ceramide accumulation in the retina, causing a degenerative phenotype that recapitulates clinical features of retinitis pigmentosa (14). This underscores AdipoR1's pivotal role in preserving retinal health by regulating ceramide balance. However, the effect of the products resulting from AdipoR1's ceramidase activity, namely sphingosine (SPH) and free FAs, on other proteins involved in lipid metabolism in the retina remains unexplored. While FAs and their derivatives can serve as ligands for the PPARα receptor, a central regulator of lipid metabolism (15, 16), existing evidence suggests a distinctive dynamic. It was shown that AdipoR2, not AdipoR1, appears to stimulate PPARα in the liver. Conversely, AdipoR1 seems to have a stronger association with activating the AMPK pathway (17). Still, it remains undetermined whether the same signaling-pathway dynamics orchestrated by AdipoR1 in the liver are replicated in the retina, necessitating further investigative endeavors to elucidate this aspect.

Considering AdipoR1 as a lipid-metabolism regulator, there seems to be a robust connection between AdipoR1, ceramide, and FA metabolism. While we have gained insights into AdipoR1's role, its specific function in PUFA metabolism, which is crucial for neural tissues such as the retina, remains unclear. Prior studies indicate that *AdipoR1* deletion in mice results in a marked decrease of docosahexaenoic acid (DHA) and of other PUFAs linked to certain phosphatidylcholine (PC) species within the retina (18–20). It has also been documented that AdipoR1 and AdipoR2 double-KO mice exhibit embryonic lethality due to extreme saturation of the phospholipids in membranes, which diminishes the lipid bilayer's fluidity (21). However, understanding the role of AdipoR1 in the retina, where it is abundantly expressed and where the lack of the functional receptor has pronounced adverse effects, requires a comprehensive and holistic analysis of the changes in lipid and PUFA composition in the retinas of *AdipoR1*$^{-/-}$ mice *versus* WT mice.

Accordingly, we sought to investigate AdipoR1's role in PUFA and lipid metabolism in the retina, RPE, and brain, to examine the potential therapeutic benefits of modulating these systems. We conducted lipidomic, transcriptomic, and proteomic examination of the retinas from *AdipoR1*$^{-/-}$ mice and probed for changes in retinal structure through transmission electron microscopy (TEM). We further explored the effect of pharmacological inhibition of ceramide synthesis on PUFA concentrations in the mouse retina. Our findings show that the absence of the *AdipoR1* gene in *AdipoR1*$^{-/-}$ mice leads to altered PUFA profiles in the retina and RPE, characterized by decreased ω3 VLC-PUFAs and increased ω6 PUFAs. The absence of AdipoR1 also implies a disrupted PPARα signaling pathway, likely affecting PUFA transport and oxidation. Using a ceramide metabolism-targeting approach in these mice, we effectively restored ω3 PUFA levels and enhanced retinal structure and function. Moreover, the study unveiled a potential connection between AdipoR1, the Bardet-Biedl syndrome (BBSome) complex, and the function of the photoreceptor cilium.

Results

Untargeted lipidomic analysis of the retina and brain of AdipoR1$^{-/-}$ *mice*

Although AdipoR1 is integral to lipid metabolism, its specific impact on diverse lipid classes, their interacting proteins, and their relationships remain unknown (9) (18, 20, 22). In this study, we provide an in-depth analysis of the lipidomic profiles in the retina, RPE, and brain of *AdipoR1*$^{-/-}$ mice to elucidate the dynamics of lipid metabolism within these tissues. The brain was selected as a reference tissue, given the distinct expression patterns of *AdipoR2*, highlighting the varied roles these receptors play in different tissues. The retina, showing marginal *AdipoR2* expression, serves as a critical site to examine the unique effects of *AdipoR1* deficiency on lipid metabolism (9). We performed untargeted lipidomic analysis on the retinas, RPE cells, and brains of *AdipoR1*$^{-/-}$ mice and their WT littermates at postnatal day 30 (P30) (Fig. 1).

Our untargeted lipidomic approach, employing liquid chromatography coupled with high-resolution mass spectrometry, enabled the identification of over 20 lipid classes. From these, we focused on 19 classes comprising at least three species. These lipid classes can be categorized into three main groups: (i) phospholipids, which include PC, phosphatidylethanolamine (PE), phosphatidylserine, phosphatidylinositol, phosphatidylglycerol, phosphatidic acid, lyso-phosphatidylcholine (LPC), and lyso-phosphatidylethanolamine (LPE); (ii) sphingolipids, encompassing ceramide, hexosyl-ceramides (Hex1Cer and Hex2Cer), sphingomyelin (SM), and SPH; and (iii) neutral lipids, comprising diglyceride (DG), triglyceride (TG), acylcarnitine (AcCa), monoglyceride, cholesterol ester (ChE), and wax monoester. In the retinas of *AdipoR1*$^{-/-}$ mice (Fig. 1*A*), we observed an increase relative to WT in hexosyl-1-ceramide (2.04-fold, P_{adj} =0.0082), TG (1.71-fold, P_{adj} =0.0384), SM (1.4-fold, P_{adj} = 0.0034) and a decrease in DG (−1.89-fold, $P_{adj} < 0.0001$), AcCa (−1.92-fold, P_{adj} = 0.0265), and LPE (−1.54-fold, P_{adj} = 0.0268). In the RPE (Fig. 1*B*), we found increased levels of PE (1.36-fold, P_{adj} = 0.0187) and ChE (1.68-fold, P_{adj} = 0.0471) and a decrease in LPC (−1.41-fold, P_{adj} = 0.0487). No significant changes were observed in the lipid classes of the brain samples (Fig. 1*C*). Although the increase in total ceramide levels within the retina and RPE cells displayed a trend towards accumulation, it did not reach statistical significance, highlighting a nuanced elevation of specific ceramide species rather than a uniform increase across the entire ceramide class (Fig. 1, *D* and *E*).

To discern the global variations among individual lipid species, we visualized them using volcano plots (Fig. 1, *F* and *G*). We identified 746, 824, and 1171 lipid species in the retina,

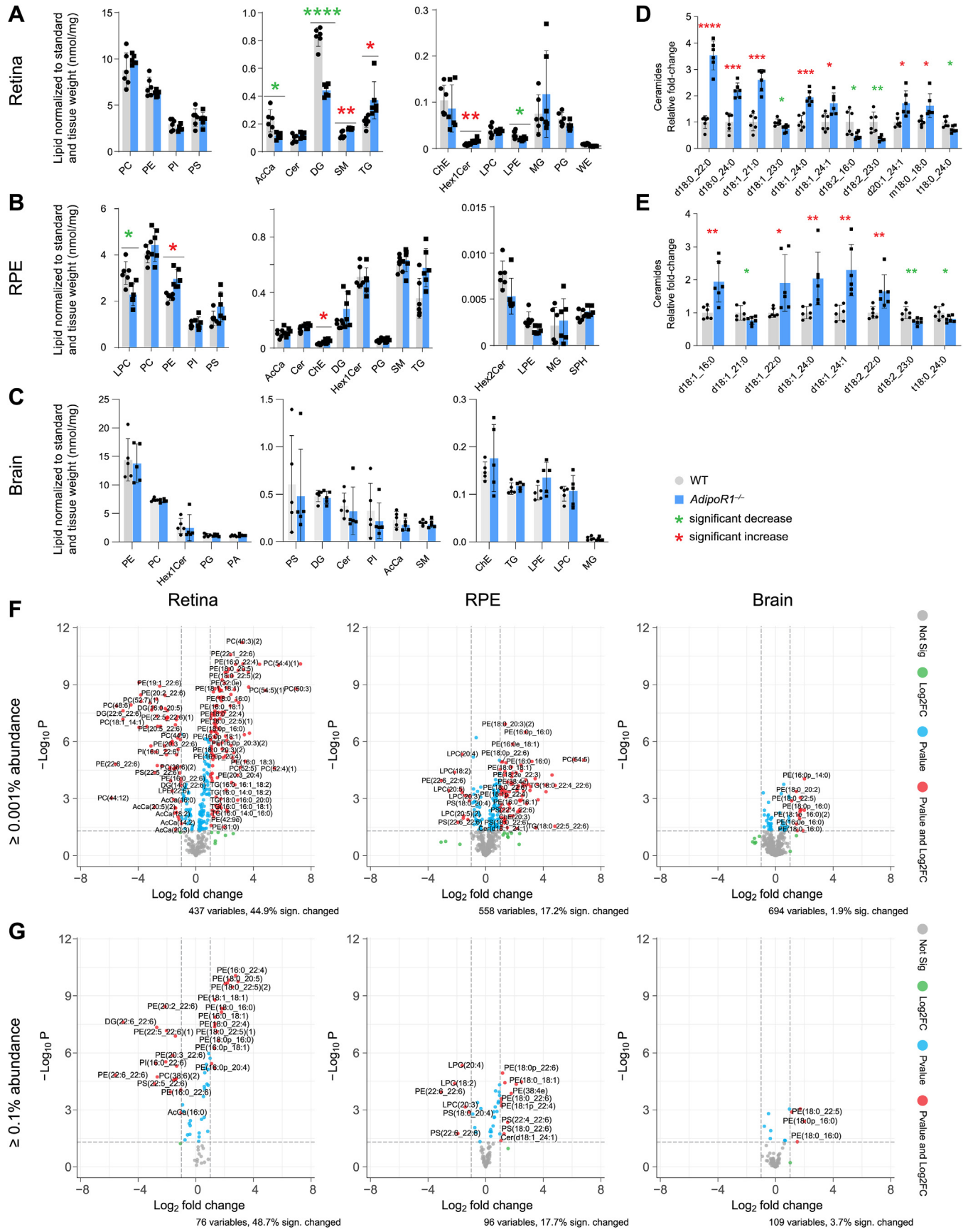

Figure 1. Untargeted lipidomic analysis of neural retina, RPE cells, and brain of *AdipoR1*$^{-/-}$ mice. Lipid-class profiles are shown for (*A*) the neural retina (n = 6), (*B*) RPE cells (n = 5), and (*C*) brains (n = 5) of 1-month *AdipoR1*$^{-/-}$ and WT mice. Data represent the mean ± SD. *D* and *E*, significantly changed ceramides in (*D*) retina and (*E*) RPE cells of WT and *AdipoR1*$^{-/-}$ mice. Data represents the mean ± SD; n = 6 for each genotype. *F* and *G*, volcano plots show

RPE, and brain, respectively. From them, we focused on species with a relative abundance of at least 0.001% (Fig. 1*F*). Among these, about 45% of species in the retina, 17% in the RPE, and under 2% in the brain exhibited significant alterations ($P_{adj} < 0.05$ and $|\log_2 FC| \geq 1$) in *AdipoR1*$^{-/-}$ mice (Fig. 1*F*, red dots). Consequently, the most pronounced changes were evident in the retina, followed by the RPE, while the brain exhibited only small variations. In the retina, the observed lipid profile alterations included 124 lipids increasing in content and 72 decreasing due to the absence of AdipoR1. The classes that showed the greatest changes were PE, PC, TG, and DG, with 74, 54, 22, and 18 lipid species changed, respectively. Similarly, 96 lipids were altered in the RPE, with 83 upregulated and 13 downregulated. The most notable changes were observed in the PE, TG, PC, and ChE classes, with 21, 16, 6, and 5 species affected, respectively.

In the retinas of *AdipoR1*$^{-/-}$ mice, the largest decrease (−333-fold, $P_{adj} < 0.0001$) was observed for TG 22:6/22:6/22:6, followed by a −59-fold decrease of PC 22:6/22:6 ($P_{adj} = 0.0009$) and a −48-fold decrease of PE 22:6/22:6 ($P_{adj} < 0.0001$). In the RPE, the most substantial decreases were in PE 22:6/22:6 (−8.5-fold, $P_{adj} = 0.0016$), LPC 20:5 (−5.9-fold, $P_{adj} = 0.0024$), and LPC 18:2 (−4.5-fold, $P_{adj} = 0.0033$). The species most increased in the retina were PC 54:7 (154-fold, $P_{adj} < 0.0001$), PC 50:3 (126-fold, $P_{adj} = 0.0002$), and PC 54:4 (54-fold, $P_{adj} = 0.0036$); and in the RPE, the most decreased were PC 52:4 (113-fold, $P_{adj} = 0.0004$), PC 54:5 (72-fold, $P_{adj} = 0.0005$), and TG 18:0/22:4/22:6 (28-fold, $P_{adj} = 0.0023$). The following lipid species were among the most increased in both retina and RPE: PC 52:4, PC 54:5, PE 18:0/22:3, and PE 16:0/14:0. Notably, 10 out of 20 of the most elevated species in the RPE were TGs, containing one or two DHA (22:6) acyl chains. In the brain of *AdipoR1*$^{-/-}$ mice, 13 lipid species changed compared to WT, increasing between 2.2- and 4-fold. Except for one LPE species, all other lipids belonged to the PE class, with PE 16:0/14:0 being the most elevated. Three species, PE 18:0/22:3, PE 16:0/14:0, and PE 16:0/16:0, were increased in all three tissues: retina, RPE, and brain.

Next, we analyzed the distribution of lipids based on their unsaturated-bond count in the neural retina and RPE cells of both WT and *AdipoR1*$^{-/-}$ mice (Fig. S1). Our findings indicated increases in saturated (1.6-fold, $P_{adj} = 0.0395$), monounsaturated (1.8-fold, $P_{adj} < 0.0001$), and di-unsaturated lipids (1.5-fold, $P_{adj} = 0.0011$) in the retina. Conversely, lipids with three or more unsaturated bonds decreased by −1.2-fold ($P_{adj} = 0.0395$), as shown in Fig. S1*A*. In the RPE, there was a notable −1.75-fold decrease in di-unsaturated lipids ($P_{adj} < 0.0001$), as presented in Fig. S1*B*.

Altered PUFA profiles in the retina and RPE cells of AdipoR1$^{-/-}$ *mice*

To elucidate the role of PUFAs in the context of retinal health and potential disease pathways, especially given their fundamental significance in retinal development and function (14), we undertook an extensive analysis of PUFA content in the retina and RPE of *AdipoR1*$^{-/-}$ mice. We analyzed total PUFAs, encompassing esterified and free species. In the retina, we observed a diminution in the levels of LC- and VLC-PUFAs (Fig. 2, *A*–*C*). Particularly noteworthy was the marked decrease in all ω3 PUFAs that contain six unsaturated bonds, ranging from 22:6 to 36:6. The most substantially decreased were ω3 VLC-PUFAs such as 32:6n3 (−167-fold, $P_{adj} = 0.0003$), 30:6n3 (−125-fold, $P_{adj} = 0.0004$), and 34:6n3 (−50-fold, $P_{adj} = 0.0006$) and VLC-PUFAs that contain five unsaturated bonds such as 30:5 (−48-fold, $P_{adj} = 0.0002$), 28:5 (−12-fold, $P_{adj} = 0.0002$). Conversely, several ω6 PUFA species accumulated in the retina. These included 36:4n6 (70-fold, $P_{adj} = 0.0007$), 24:4n6 (2.2-fold, $P_{adj} = 0.0005$), 22:4n6 (2-fold, $P_{adj} = 0.0049$), 34:4n6 (2-fold, $P_{adj} = 0.0321$), 26:4n6 (1.6-fold, $P_{adj} = 0.011$), and arachidonic acid (AA, 20:4n6; 1.4-fold, $P_{adj} = 0.0304$). Additionally, there were increased levels of certain PUFAs, like 36:5 (4.9-fold, $P_{adj} = 0.0025$) and 18:3 (4.2-fold, $P_{adj} = 0.0001$).

In the RPE, a similar pattern was observed with the largest decrease in ω3 PUFAs being 32:6n3 (−63-fold, $P_{adj} = 0.0112$) and 34:6n3 (−22-fold, $P_{adj} = 0.0486$) and an accumulation of ω6 PUFAs such as 36:4n6 (505-fold, $P_{adj} = 0.0024$), 34:4n6 (20-fold, $P_{adj} = 0.0002$), and 36:5 (12-fold, $P_{adj} = 0.0005$) (Fig. 2, *A* and *D*). However, there was a significant difference in the levels of DHA between the RPE and retina; in the RPE, DHA was increased 1.9-fold ($P_{adj} = 0.0123$), whereas in the retina, DHA was decreased −2.4-fold ($P_{adj} = 0.0003$). Therefore, we utilized a volcano plot to visualize changes in DHA-containing lipids within the retina and RPE (Fig. S2*A*). This display revealed a divergent trend in the TG alterations across the two tissues (Fig. S2*B*). Specifically, among the 34 DHA-containing lipids in the RPE that showed significant changes, 25 were TGs. These TGs showed increases ranging from 3.8-fold to 30.4-fold. Conversely, in the retina, the pattern was reversed; of the 46 significantly altered DHA-comprising lipids, 37 were decreased, including 12 TGs, which showed decreases ranging from −2.5-fold to −333-fold. The increases in TGs in the RPE could mean that DHA was being stored in the RPE rather than mobilized and transported to the photoreceptors.

Considering the mounting evidence highlighting the significance of the ω6 to ω3 PUFA ratio (23–25), particularly regarding retinal inflammation observed in *AdipoR1*$^{-/-}$ mice prior to the onset of photoreceptor degeneration (9), we calculated the ω6/ω3 ratio in the *AdipoR1*$^{-/-}$ and WT samples.

significant alterations in the lipidome of the retinas and RPE cells but not the brains of the *AdipoR1*$^{-/-}$ mice. *F*, lipid species whose relative abundance was ≥ 0.001%. *G*, lipid species whose relative abundance was ≥ 0.1%. The species above the significance threshold ($p < 0.05$ and $|\log_2 FC| \geq 1$) are highlighted in *red*, comprising 44.9%, 17.2%, and 1.9% of the total lipids in the retinas, RPE cells, and brains, respectively. In (*A*–*E*), statistical significance was determined with a 2-tailed *t* test analysis followed by *p*-value adjustment by Holm–Sidak's multiple comparison corrections: *$p < 0.05$, **$p < 0.01$, ***$p < 0.001$, ****$p < 0.0001$. AcCa, acylcarnitine; Cer, ceramides; ChE, cholesterol ester; DG, diglyceride; Hex1Cer, hexosyl-ceramides; LPC, lyso-phosphatidylcholine; LPE, lyso-phosphatidylethanolamine; MG, monoglyceride; PA, phosphatidic acid; PC, phosphatidylcholine; PE, phosphatidylethanolamine; PG, phosphatidylglycerol; PI, phosphatidylinositol; PS, phosphatidylserine; RPE, retinal pigmented epithelium; SM, sphingomyelin; SPH, sphingosine; TG, triglyceride; WE, wax monoesters.

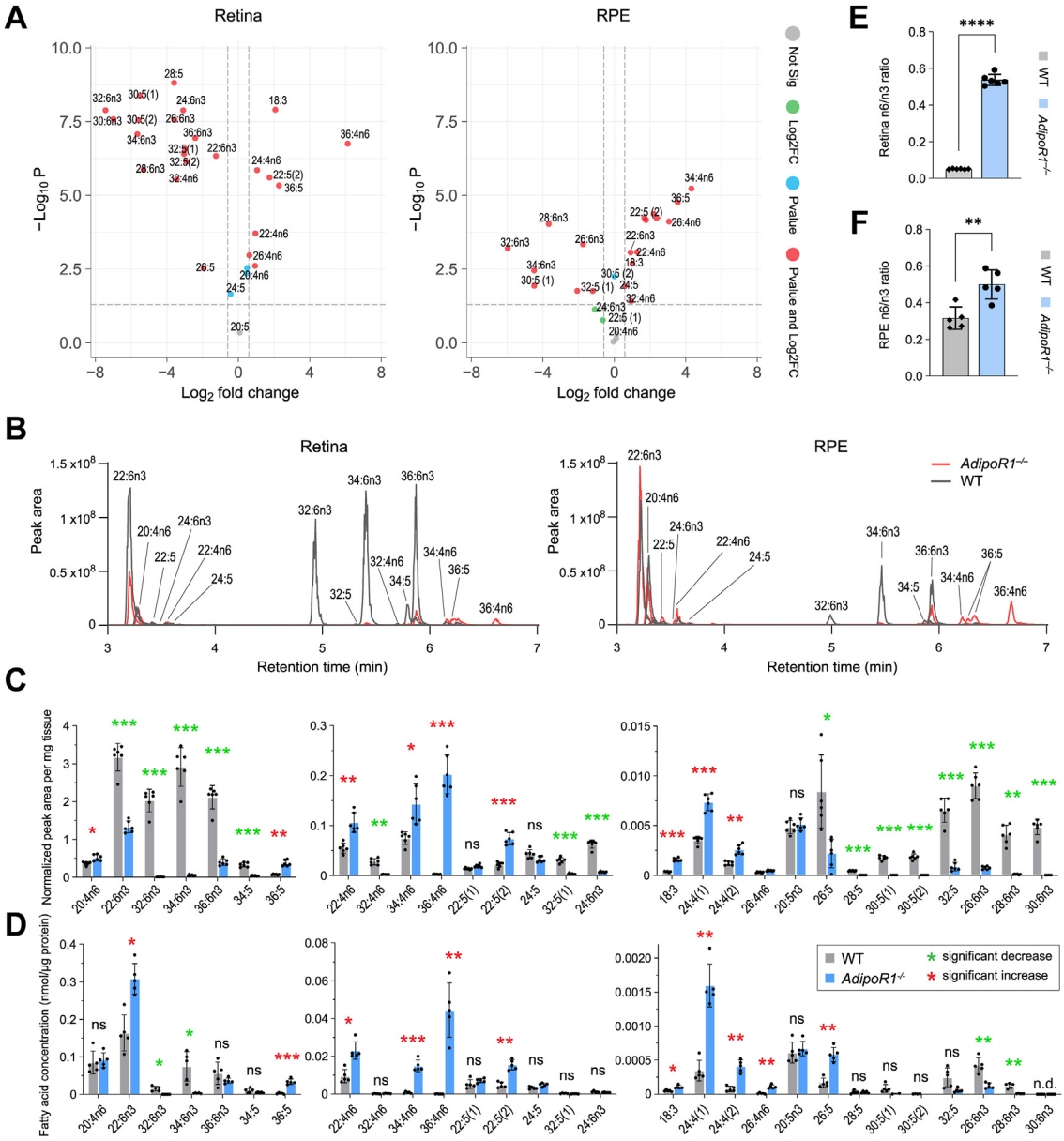

Figure 2. Polyunsaturated fatty acids levels in the retina and RPE cells of *AdipoR1*$^{-/-}$ mice. *A*, volcano plots display significant changes in total (free and esterified) PUFA levels in the retina (*left*) and RPE cells (*right*) of 1-month *AdipoR1*$^{-/-}$ mice. *B*, extracted ion chromatograms (EIC) of PUFAs in the retina (*left*) and RPE cells (*right*). *C* and *D*, relative levels of PUFAs in the retina (*C*) and RPE cells (*D*) of 1-month *AdipoR1*$^{-/-}$ mice. *E* and *F*, comparison of the ω6 to ω3 PUFA ratio in the retina (*E*) and RPE cells (*F*) of *AdipoR1*$^{-/-}$ mice. Specific FAs measured included ω6 PUFAs (20:4, 22:4, 26:4, 32:4, 34:4, 36:4) and ω3 PUFAs (22:6, 24:6, 26:6, 28:6, 32:6, 34:6, 36:6). In (*C*–*F*), data represent the mean ± SD, with n = 6 per genotype for analysis of retinas and n = 5 for RPE. Statistical significance in (*C* and *D*) was determined using a 2-tailed *t* test with *p* value adjustment by Holm–Sidak's multiple comparison correction and in (*E* and *F*) using a 2-tailed *t* test: *$p < 0.05$, **$p < 0.01$, ***$p < 0.001$, ****$p < 0.0001$. PUFA, polyunsaturated fatty acid; RPE, retinal pigmented epithelium.

Our findings revealed a substantial elevation in the ω6/ω3 ratio, which was 10.5-fold higher in the retina ($p < 0.0001$; Fig. 2*E*) and 1.6-fold higher in the RPE ($p = 0.0035$; Fig. 2*F*) of *AdipoR1*$^{-/-}$ mice *versus* WT.

Based on our observations, AdipoR1 plays a significant role in regulating PUFA levels in the retina and RPE, influencing the balance between ω3 and ω6 PUFAs. This regulatory role could involve mechanisms related to ω3 PUFA synthesis and uptake and the transport of DHA from RPE to photoreceptors. However, it is important to note that these findings derive from studies using whole-body KO mice, which cannot distinguish cell-autonomous effects. Therefore, while our data suggest a crucial role for AdipoR1, further tissue-specific investigations are needed to determine its direct impact on these processes specifically within the eye.

Changes in lipid metabolism and storage in the RPE of AdipoR1$^{-/-}$ *mice*

We performed lipid ontology (LO) analysis to gain insight into the molecular mechanisms underlying the role of AdipoR1 in lipid metabolism in the retina and RPE (Fig. 3, *A* and *B*). The retina of *AdipoR1*$^{-/-}$ mice showed significant enrichment of LO terms related to mitochondria, plasma membrane,

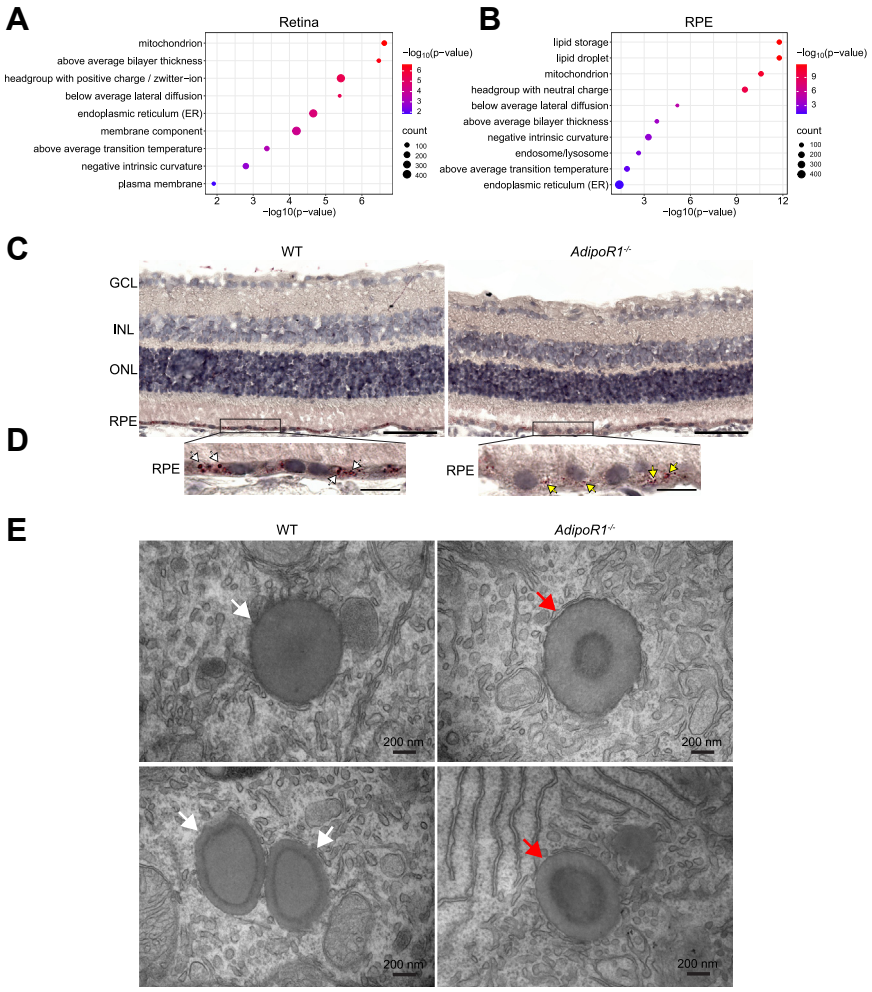

Figure 3. Altered lipid droplets and atypical deposits found in the RPE of *AdipoR1*$^{-/-}$ mice. *A* and *B*, lipid enrichment ontology analysis in the retinas (*A*) and RPE cells (*B*) of 1-month *AdipoR1*$^{-/-}$ mice. *C*, frozen cross-sections of retinas from *AdipoR1*$^{+/+}$ (WT) and *AdipoR1*$^{-/-}$ mice, stained with oil Red-O and hematoxylin; scale bar represents 50 μm. *D*, higher magnification of RPE cross-sections from (*C*), showing normal (*white* arrow) and reduced size (*yellow* arrow) lipid droplets; scale bar represents 10 μm. *E*, electron microscopy images indicate atypical type-A deposits found in the RPE of 1-month *AdipoR1*$^{-/-}$ mice (*upper* and *lower right*; *red* arrows) that are different from type-A–like deposits found in age-matched WT controls (*upper* and *lower left*; *white* arrows); scale bar represents 200 nm. RPE, retinal pigmented epithelium.

and endoplasmic reticulum (Fig. 3*A*), suggesting altered lipid metabolism and transport, particularly in these cellular components. The terms related to the physical properties of the lipid bilayer, such as increased bilayer thickness, below-average lateral diffusion, above-average transition temperature, and negative intrinsic curvature, suggest that the absence of AdipoR1 impacts the mechanical properties and fluidity of the lipid bilayer, which affect the overall function of the retina. The changes of charged headgroups (positive charge/zwitterion) may indicate changes in lipid signaling and interactions with proteins, but we did not investigate this aspect in detail. In the RPE cells of *AdipoR1*$^{-/-}$ mice, the most enriched LO terms were related to lipid storage, lipid droplets (LDs), mitochondria, and headgroups with a neutral charge (Fig. 3*B*), suggesting altered lipid metabolism and storage. Overall, the above data show a different distribution of lipid headgroups and altered physical properties of the lipid bilayer in the retinas and RPE as a consequence of AdipoR1 ablation, confirming the crucial contribution of AdipoR1 in promoting lipid homeostasis of these tissues.

Next, we studied the LDs in the RPE using Oil Red-O (ORO), a fat-soluble dye that binds to neutral lipids and cholesteryl esters, to stain retinal cross-sections. The primary neutral lipids of the LD core, which are called retinosomes in the RPE, are retinyl esters, ChEs, and TGs (26–28). We found that the LDs in *AdipoR1*$^{-/-}$ mice were significantly smaller than those in WT mice (Fig. 3*C*). This finding coincides with our lipid ontology data, confirming altered lipid storage and trafficking in RPE as a consequence of AdipoR1 absence. Moreover, this result agrees with our previous observation in *AdipoR1*$^{-/-}$ mice (9) of significantly decreased retinyl esters, the major component of retinosomes (29). This observation could partially explain the smaller LDs observed in the RPE of the *AdipoR1*$^{-/-}$ mice.

Alterations in cell morphology of the RPE and photoreceptors in the absence of AdipoR1

Next, we studied the impact of the lipid changes in the retina of *AdipoR1*$^{-/-}$ mice on the ultrastructure of RPE and

photoreceptors using TEM. In the RPE, images revealed atypical deposits (here named type-A deposits) that were present in the RPE of approximately 1-month *AdipoR1*$^{-/-}$ mice (Fig. 3*E*, upper and lower right), which were different from the type-A–like deposits seen in age-matched WT controls (Fig. 3*E*, upper and lower left). Specifically, type-A deposits in the RPE of the *AdipoR1*$^{-/-}$ mice exhibited an electron-dense core with a prominent ring, while in age-matched WT controls, the core was less electron-dense, and the ring rim was narrower. Moreover, type-A deposits exhibited increased heterogeneity in size and shape (Fig. S3). The different ultrastructure of the atypical deposits found in the RPE of *AdipoR1*$^{-/-}$ mice suggests an abnormal accumulation of substances that the cells in this tissue do not process or clear correctly, such as abnormal protein aggregates or mineralization within the lipid deposits. Type-B deposits in the RPE of *AdipoR1*$^{-/-}$ and WT mice were similar and contained homogenous electrodense material (Fig. S4).

TEM images of photoreceptors showed significantly shorter rod outer segments (ROSs) in *AdipoR1*$^{-/-}$ mice (Fig. 4*A*) compared to their WT counterparts (Fig. 4*B*). Moreover, we observed a mix of normal and disorganized ROSs in the *AdipoR1*$^{-/-}$ mice that were not present in WT littermates. Some photoreceptors displayed normal disk morphology at the base (Fig. 4, *C* and *D*), but the disks in other parts of the OSs were disorganized. Furthermore, we observed dysmorphic OSs in *AdipoR1*$^{-/-}$ mice that contained electro-lucent spherical or irregular vesicles (Fig. 4*C*). These vesicles were not present in the WT mice (Fig. 4*E*), which exhibited tightly packed and highly organized disks (Fig. 4*E*).

Interdigitations of the ROS and the apical processes of the RPE cells ensure homeostasis for the biochemistry of vision. The morphology of the RPE apical processes in *AdipoR1*$^{-/-}$ mice (Fig. 4*F*) and WT mice (Fig. 4*G*) appeared normal; however, in the *AdipoR1*$^{-/-}$ mice, the microvilli were more relaxed and extended into the subretinal space, where the ROSs were shortened as observed by light microscopy (Fig. 3*C*). We did not observe apparent differences in the ultrastructure of the photoreceptor mitochondria between the two strains. Notably, the presence of phagocytosed ROSs within the RPE cells of both the *AdipoR1*$^{-/-}$ (Fig. 4, *J* and *K*) and WT mice (Fig. 4*L*) indicates that the absence of AdipoR1 does not hinder the ability of RPE cells to phagocytose the ROS; however, we do not know its impact on the efficiency of the phagocytosis.

RNA-seq suggests downregulation of PPARα-mediated fatty acid transport in the RPE cells of AdipoR1$^{-/-}$ *mice*

To investigate how the absence of AdipoR1 affects gene expression related to lipid metabolism, we re-analyzed our bulk RNA-seq data from the retina and RPE cells of *AdipoR1*$^{-/-}$ mice (9). In the retina of WT mice, the expression of the *AdipoR1* gene was 7.3-fold higher than that of *AdipoR2* ($P_{adj} < 0.0001$) (Fig. S5*B*). Conversely, in the RPE of WT mice, the expression levels of *AdipoR1* and *AdipoR2* were comparable (Fig. S5*C*). Notably, the ablation of *AdipoR1* did not alter *AdipoR2* expression in either the retina or RPE (Fig. S5, *B* and *C*).

While previous research has linked AdipoR2 predominantly with the stimulation of PPARα and AdipoR1 with activating the AMPK pathway in the liver (17), we re-evaluated the potential involvement of AdipoR1 in modulating the PPARα pathway in the retina. Our findings in the RPE document shifts in PPARα-mediated lipid and FA metabolic signaling in *AdipoR1*$^{-/-}$ mice (Fig. 5, *A* and *B*). We found downregulation of genes involved in FA binding, transport, and metabolism, such as *Mfsd2a, Fabp1, Slc27a2, Slc27a5, Apoa1, Apoa2, Fads2, Ppara*, and *Hmgcs1*. The most downregulated genes were *Fabp1* (−26.5-fold, P_{adj} = 0.0034), *Slc27a2* (−8.2-fold, P_{adj} = 0.0088), and *Mfsd2a* (−2.9-fold, $P_{adj} < 0.0001$). *Fabp1* encodes for an FA-binding protein that enables the intracellular transport of FAs, while Slc27a2, also known as FA transport protein 2 (FATP2), facilitates the transport of FAs across cellular membranes. Slc27a2 is an acyl-CoA ligase, triggering the ATP-dependent production of fatty acyl-CoA using FAs as substrates. This function impedes the efflux of FAs from cells and potentially promotes more FA uptake (30, 31). Also, we observed the downregulation of *Mfsd2a*, which encodes an LPC transporter crucial for the uptake of DHA, a key lipid for building ROS membranes (13, 32, 33). *Mfsd2a* downregulation is consistent with the observed lower levels of LPCs in the RPE (Fig. 1*B*).

Moreover, in the RPE of *AdipoR1*$^{-/-}$ mice, we observed a significant shift in the expression of genes related to LD formation and FA storage. Notably, *Acsbg1*, encoding for acyl-CoA synthetase bubblegum-family member 1, was increased 3.2-fold (P_{adj} = 0.0082). This enzyme is known to activate VLC-FA, suggesting an adaptive response to altered FA metabolism in the absence of AdipoR1. Similarly, the 2-fold increase in *Plin2* and *Plin4* (P_{adj} = 0.0005 and 0.0082, respectively) might suggest enhanced demand for lipid storage within LDs. *Plin2* and *Plin4*, as members of the perilipin family, play critical roles in regulating LD formation and protecting lipids from hydrolysis, indicating a possible compensatory mechanism for disrupted FA metabolism and transport. These alterations suggest that AdipoR1 deficiency impacts FA transport and metabolism but also triggers adaptive changes in lipid storage mechanisms in the RPE.

While the changes in the retina were more subtle than those in the RPE, they still provided valuable insights. We detected a downregulation in *Ppara* expression (−2-fold, P_{adj} = 0.0122), but no changes were observed in *Ppard* or *Pparg* (Fig. S5*A*). *Elovl2* and *Elovl4*, involved in FA elongation, showed relatively small decreases in expression, with values of −1.5-fold (P_{adj} = 0.0237) and −1.4-fold (P_{adj} = 0.0013), respectively. Interestingly, there was an upregulation in the FA desaturase family, with *Fads2* (2.2-fold, $P_{adj} < 0.0001$), *Fads1* (1.3-fold, P_{adj} = 0.0051), and *Fads3* (1.4-fold, P_{adj} = 0.0318) showing increased expression. Additionally, the expression of stearoyl-Coenzyme A desaturase 1 (*Scd1*) was increased by 3.9-fold ($P_{adj} < 0.0001$). Scd1 is pivotal in converting saturated FAs to monounsaturated FAs (34). Its marked upregulation in the *AdipoR1*$^{-/-}$ retina may underlie the observed rise in monounsaturated FA levels (Fig. S1*A*). Overall, these findings reinforce the concept of AdipoR1 as a key molecular player necessary in lipid metabolism and transport in the RPE and neural retina.

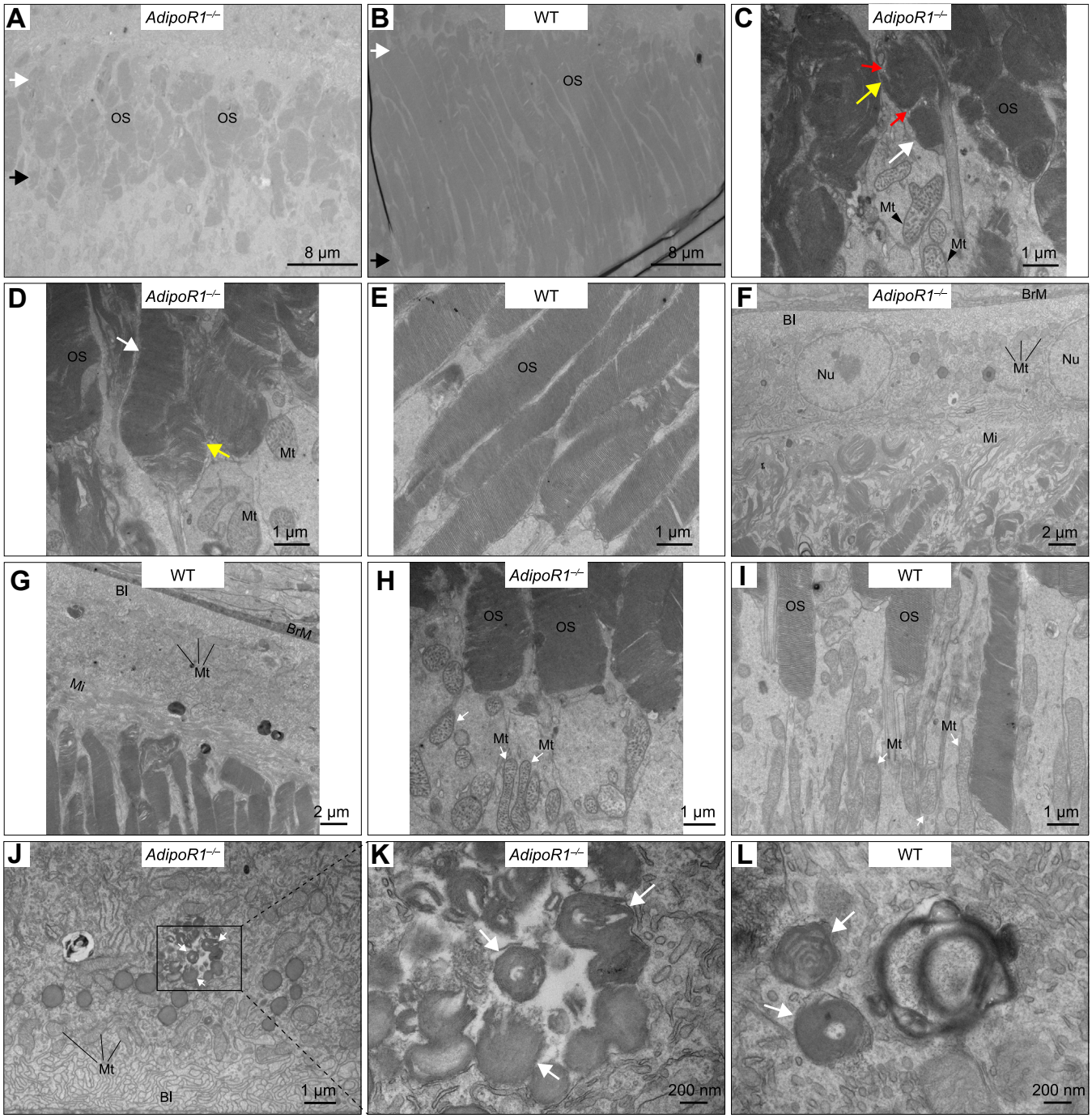

Figure 4. Transmission electron microscopy of photoreceptors and RPE cells of *AdipoR1*$^{-/-}$ and WT mice. *A*, photoreceptor outer segments in 1-month *AdipoR1*$^{-/-}$ mice are shorter and consist of normal (not disorganized) and disorganized ROS, when compared to (*B*) age-matched WT control. *White* arrows indicate the distal parts, and *black* arrows point to the proximal parts of the photoreceptor OS. *C*, normal disks at the *bottom part* (*white arrow*) and disorganized discs at the upper part of the OS (*yellow arrow*) in *AdipoR1*$^{-/-}$ mice. We observed electro-lucent spherical or irregular vesicles (*red arrows*) in the middle of the ROS from *AdipoR1*$^{-/-}$ mice, which were rarely seen between disks from WT mice. *D*, photoreceptor OS with two rows of disks—normal disks in the apex (*white arrow*) and disorganized discs at the bottom of the OS (*yellow arrow*) in *AdipoR1*$^{-/-}$ mice. *E*, normal ROS with highly organized disks in a WT B6-albino mouse. *F* and *G*, RPE apical processes in *AdipoR1*$^{-/-}$ mice (*F*) and WT mice (*G*). The microvilli in *AdipoR1*$^{-/-}$ mice appeared normal, except they were more relaxed and extended into the subretinal space, where the ROSs were shortened. *H* and *I*, the morphology of photoreceptor mitochondria was similar in *AdipoR1*$^{-/-}$ mice (*H*) and WT mice (*I*). *J–L*, phagocytosed ROSs (*white* arrows) in the RPE of *AdipoR1*$^{-/-}$ mice (*J* and *K*) and WT mice (*L*). In *panels C*, *D*, and *H*, note that vertical-cut OSs are rare due to disorganization. Thus, the morphology of the whole ROS (basal to tip) is unknown for most ROSs. Bl, basal infoldings; BrM, Bruch's membrane; Mi, microvilli; Mt, mitochondria; Nu, nucleus; OS, photoreceptor outer segment; ROS, rod outer segment; RPE, retinal pigmented epithelium.

Proteome profiling reveals disrupted fatty acid metabolism and photoreceptor function in AdipoR1$^{-/-}$ *mice*

To further investigate the effects of AdipoR1 on FA metabolism and to corroborate the above findings, we conducted proteomic analyses on the neural-retina and RPE-eyecup samples from *AdipoR1*$^{-/-}$ mice. We identified 2045 proteins in the neural retina and 1765 in the RPE. Of these, 206 proteins (10.1%) in the retina and 63 proteins (3.6%) in the RPE

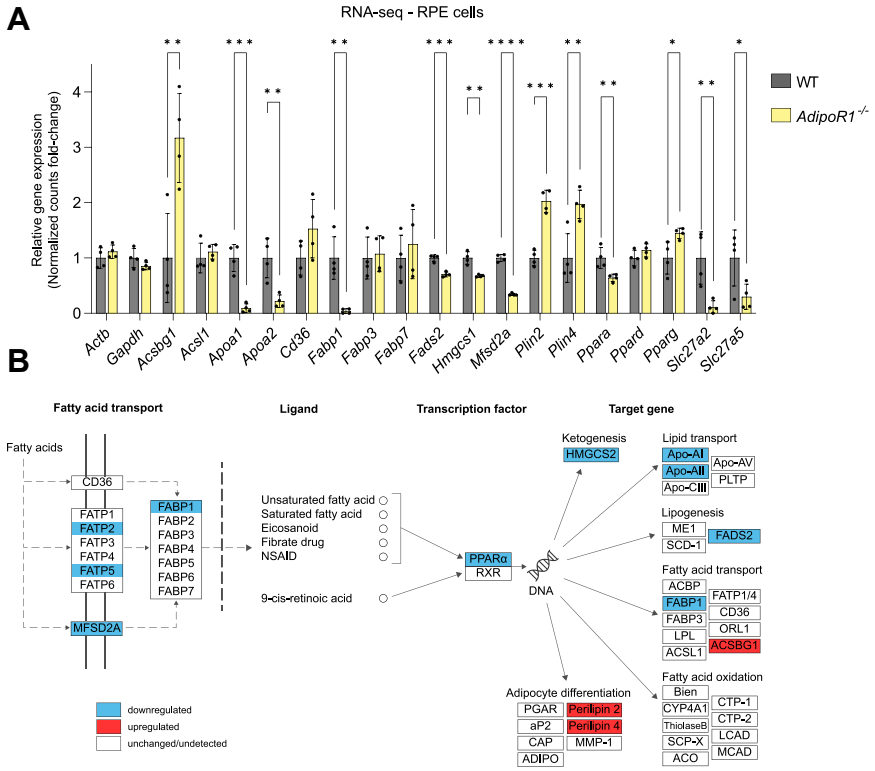

Figure 5. RNA-seq data indicate affected PPARα signaling related to changes in lipid metabolism and fatty acid transport in the RPE cells of *AdipoR1*$^{-/-}$ *versus* WT mice. *A*, relative expression levels of genes related to the PPARα signaling pathway in the RPE of *AdipoR1*$^{-/-}$ *versus* WT mice. Data represent the mean ± SD (n = 4 for each genotype at P30). The statistical significance was determined with a 2-tailed *t* test analysis. *p*-values were adjusted for multiple comparisons using the Holm–Sidak's correction method: *$p < 0.05$, **$p < 0.01$, ***$p < 0.001$, ****$p < 0.0001$. Differentially expressed genes (DEGs): *Acsbg1*, acyl-CoA synthetase bubblegum family member 1; *Apoa1*, apolipoprotein A-I; *Apoa2*, apolipoprotein A-II; *Fabp1*, FA binding protein 1; *Fads2*, FA desaturase 2; *Hmgcs1*, 3-hydroxy-3-methylglutaryl-Coenzyme A synthase 1; *Mfsd2a*, DHA transporter; *Plin2*, perilipin 2; *Plin4*, perilipin 4; *Ppara*, peroxisome proliferator activated receptor α; *Pparg*, peroxisome proliferator activated receptor γ; *Slc27a2*, solute carrier family 27 (FA transporter-a2); *Slc27a5*, solute carrier family 27 (FA transporter-a5). *B*, expression profiles of DEGs in the RPE of *AdipoR1*$^{-/-}$ mice *versus* WT mice, based on data from (*A*), visualized on the PPARα signaling pathway. The image is based on the KEGG database PPAR signaling pathway (mmu03320). DHA, docosahexaenoic acid; RPE, retinal pigmented epithelium.

exhibited significant changes, meeting the criteria of $q < 0.05$ and $|\log_2 FC| \geq 0.585$ (Fig. 6, *A* and *B*). We then examined whether the upregulated and downregulated proteins enriched specific pathways in the retina and RPE of *AdipoR1*$^{-/-}$ mice. Kyoto Encyclopedia of Genes and Genomes (KEGG) pathway analysis revealed that in the retina, the downregulated proteins were predominantly involved in phototransduction, purine metabolism, ribosome function, and PPAR pathways. In the RPE, the most downregulated pathways were related to PPAR signaling, adipocytokine signaling, FA metabolism, and peroxisome function (Fig. 6, *C* and *D*).

We further focused on the proteins involved in PPAR signaling and lipid metabolism (Fig. 6, *F* and *G*). In the retina, AdipoR1 deficiency led to a significant decrease in the proteins involved in FA transport (FABP7, −35-fold, $q = 0.0004$; FABP5, −2-fold, $q = 0.0487$; ACSL1, −1.6-fold, $q = 0.0025$), FA oxidation (CPT1A, −3.4-fold, $q = 0.0055$; ACOX1, −1.4-fold, $q = 0.0135$), and Perilipin 1 (PLIN1, −3.8-fold, $q = 0.0137$), which plays a role in LD formation. In the RPE, we found the most substantial decreases in the proteins involved in FA transport (ACSL1, −1.6-fold, $q = 0.0108$; FABP3, −2.3-fold, $q = 0.0231$; ACSL6, −1.6-fold, $q = 0.0492$; and CD36, −3.7-fold, $q = 0.0487$); FA oxidation (ACADL, −1.7-fold, $q = 0.0074$), and HMGCS2 (−2.1-fold, $q = 0.0225$), a mitochondrial ketogenesis enzyme. Adiponectin was also decreased (ADIPOQ, −2.1-fold, $q = 0.0231$). We observed that the most upregulated protein in the retina was ASAH1 (6.7-fold, $q < 0.0001$), an acid ceramidase, which plausibly compensates for the lack of AdipoR1 ceramidase. The findings suggest that AdipoR1 plays a crucial role in FA metabolism in the retina and RPE.

Our STRING analysis (35) of proteins that were significantly downregulated in the retina of *AdipoR1*$^{-/-}$ mice revealed a strong enrichment (strength > 2) in categories related to the photoreceptor OS, with a particular emphasis on the BBSome complex (Fig. 6*E*). The BBSome complex, composed of eight proteins, is crucial in regulating ciliary trafficking in primary cilia (36). It is worth noting that mutations disrupting the function of the BBSome complex lead to BBS, a genetic disorder that leads to retinitis pigmentosa in most affected people (37–39). We observed a significant decrease in the levels of several components of the BBSome complex, including BBS2 (−12.2-fold, $q < 0.0001$), BBS4 (−6.2-fold, $q = 0.0002$), BBS8 (−4.7-fold, $q < 0.0001$), BBS9 (−4.3-fold, $q < 0.0001$), and BBS7 (−2.9-fold, $q = 0.0267$) (Fig. 6, *A* and *E*).

In addition to FABP7, BBS2, and BBS4, the other top-downregulated proteins ($q < 0.0001$) in the retina included ATP-binding cassette sub-family A member 4 (ABCA4), which showed a decrease of −10.4-fold (Fig. 6*A*). There was also a

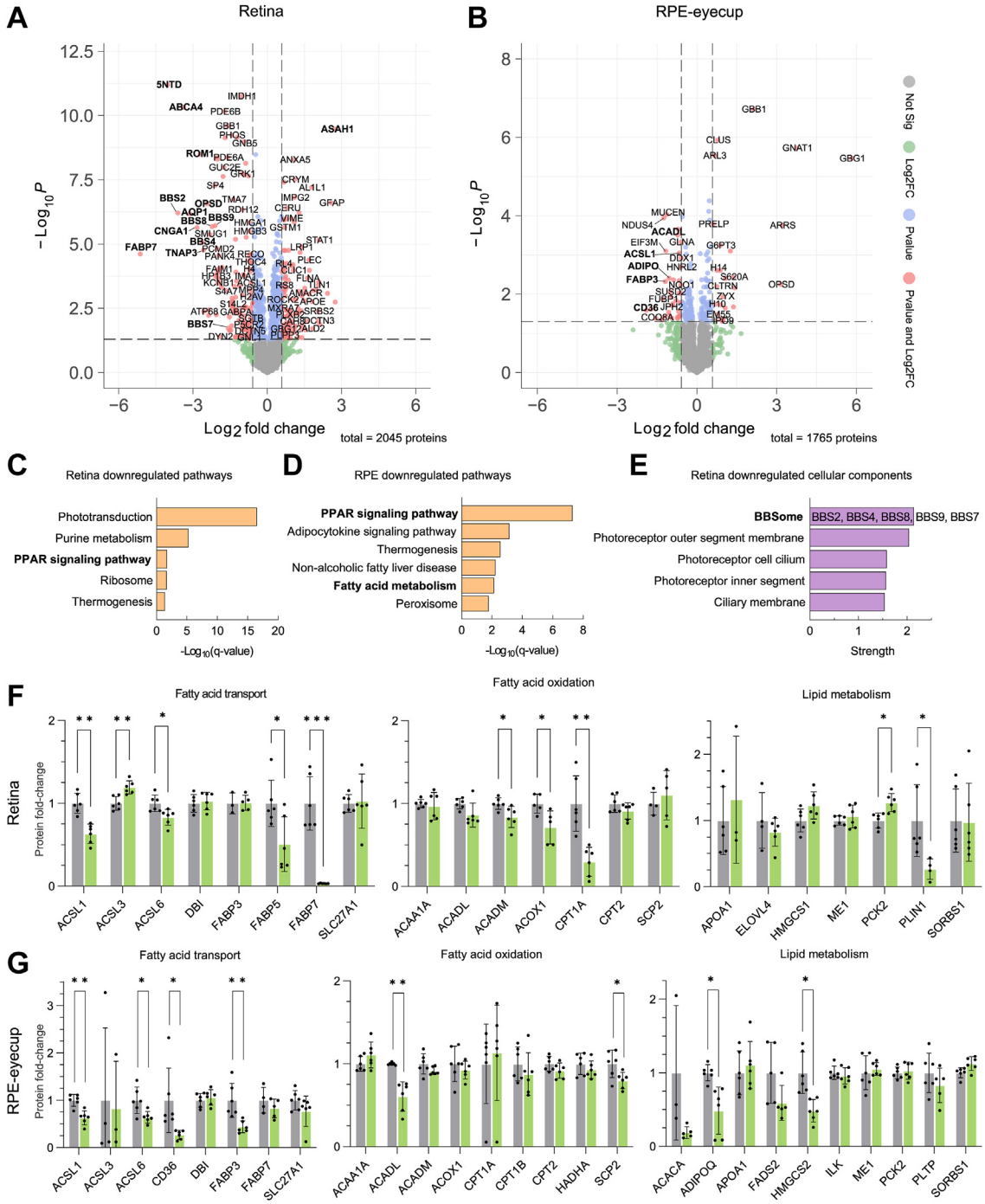

Figure 6. Proteomic analysis of retinas and RPE-eyecups of *AdipoR1*$^{-/-}$ mice. Volcano plots show significantly altered proteomes in the retina (*A*) and RPE-eyecup (*B*) of 1-month *AdipoR1*$^{-/-}$ mice. *C* and *D*, downregulated KEGG pathways in the retina (*C*) and RPE-eyecup (*D*) of *AdipoR1*$^{-/-}$ mice linked to significantly decreased protein levels (shown in *A*, *B*). *E*, STRING annotation of downregulated proteins in *AdipoR1*$^{-/-}$ mice. The Gene Ontology (GO) terms related to cellular components that show significant enrichment ($q < 0.05$) have been identified. Based on their level of enrichment, the top five GO terms are ranked and displayed in the figure. *F* and *G*, relative fold-change of the proteins engaged in FA transport, oxidation, and lipid metabolism in the retina (*F*) and RPE-eyecup (*G*) of *AdipoR1*$^{-/-}$ and WT mice. Data represent the mean ± SD for retina (n = 6 for each genotype) and RPE (n = 6 for each genotype). The statistical significance was determined with a 2-tailed *t* test. The q-value represents the false discovery rate (FDR) adjusted *p*-value, which helps control the expected proportion of incorrectly rejected null hypotheses. The *p*-values, adjusted for concurrent comparisons, employed the Benjamini, Krieger, and Yekutieli correction method. The significance levels are as follows: *$q < 0.05$, **$q < 0.01$, ***$q < 0.001$. RPE, retinal pigmented epithelium.

significant decrease in 5′-nucleotidase (5NTD, or CD73) by −16.1-fold and aquaporin-1 by −8.8-fold. Other notable changes in protein levels were cGMP-gated cation channel alpha-1 (CNGA-1), which was downregulated by −7.1-fold, ROS membrane protein 1 (ROM1) with a decrease of −6.5-fold, tumor necrosis factor alpha-induced protein 3 (TNAP3), which was decreased -6-fold, and rhodopsin (OPSD) decreased −5.4 fold.

Targeted inhibition of ceramide synthesis increases LC-PUFA levels in the RPE and retina

In our previous work (9) as well as in the current investigation, we discerned a notable accumulation of ceramides in the retina of *AdipoR1*$^{-/-}$ mice, which was linked to photoreceptor degeneration. We established a pharmacological intervention that effectively decreased ceramide levels, subsequently enhancing photoreceptor survival and visual functions in *AdipoR1*$^{-/-}$ mice. Considering the observed decrease in PUFAs herein, we hypothesized that inhibiting ceramide production could elevate PUFA levels in *AdipoR1*$^{-/-}$ mice. To examine this hypothesis, we targeted ceramide synthesis using a combination of three FDA-approved drugs, desipramine, L-cycloserine, and fingolimod (collectively termed DCF), to attenuate three major ceramide generation pathways (Fig. S6*A*). We administered the DCF mixture *via* i.p. injection three times per week for 3 weeks and then conducted optical coherence tomography and electroretinography (ERG) measurements to evaluate the retina's structure and function (Fig. S6*B*). Additionally, we performed lipidomic analyses on the retina and RPE. We found that DCF treatment increased free PUFA levels, primarily in the RPE and retina (Fig. 7). In samples of the RPE from *AdipoR1*$^{-/-}$ mice treated with DCF (Fig. 7*A*), we observed substantial elevation in several ω3-type free PUFAs, including DHA (22:6n3; 7.1-fold, P_{adj} = 0.0003), docosapentaenoic acid (22:5n3; 10.2-fold, P_{adj} = 0.0036), and eicosapentaenoic acid (20:5n3; 8.3-fold, P_{adj} = 0.0122). Additionally, free ω6 PUFAs, such as AA, (20:4n6; 2.9-fold, P_{adj} = 0.0046), adrenic acid (22:4n6; 3.9-fold, P_{adj} = 0.0116), and tetracosatetraenoic acid (24:4n6; 3.4-fold, P_{adj} = 0.0166), displayed moderate increases. Other notable elevations included PUFAs like 20:2 (2.1-fold, P_{adj} = 0.0069), 20:3 (2.4-fold, P_{adj} = 0.0069), as well as a 2-fold increase in saturated palmitic acid (16:0; P_{adj} = 0.0002). The changes in the neural retina were significant (Fig. 7*B*) but less pronounced than those in the RPE, indicating that the primary site of action of the DCF drugs was the RPE. In the neural retina, we measured a 1.8-fold increase in DHA (P_{adj} = 0.032) and a 2-fold increase in stearic acid (18:0, P_{adj} = 0.045).

To check if the increase in free PUFAs resulted in their enhanced incorporation into complex lipids, we examined lipid species esterified with DHA, the most abundant PUFA in the retina and RPE. In the RPE (Fig. 7*C*), we found a substantial elevation of DHA-containing lipids such as cholesteryl docosahexaenoate 22:6 (10.1-fold, P_{adj} = 0.011), phospholipids such as LPC 22:6 (3.6-fold, P_{adj} = 0.003), PEs (up to 8.4-fold, P_{adj} = 0.010), PIs (up to 3.4-fold, P_{adj} = 0.006), PCs (up to 2.8-fold, P_{adj} = 0.009), and glycerolipids such as DGs (up to 3.9-fold, P_{adj} = 0.029). However, the increase in TG 16:0/22:0/22:6 (15.5-fold) was not statistically significant due to high variability in these lipids (P_{adj} = 0.071). There was also an increase in some non-DHA–containing lipids, such as AcCa 20:5 (6-fold, $P_{adj} < 0.001$) and LPC 22:5 (8.5-fold, P_{adj} = 0.003). In the retina (Fig. 7*D*), the changes were smaller, showing an increase of 1.6- to 1.9-fold ($P_{adj} < 0.030$) in PE(22:5/22:6), PE(22:4/22:6), and PC(18:1/22:6).

Increasing the DHA levels in *AdipoR1*$^{-/-}$ mice treated with DCF resulted in a lowering of the AA to DHA ratio (Fig. 7*E*) in the RPE by −2.8-fold (p = 0.0002). The neural retina also displayed a similar trend with a −1.5-fold decrease, although this change was not statistically significant. Given AA's role as a pro-inflammatory FA and DHA's critical contribution to retinal health and its anti-inflammatory properties, this modulation in FA profiles suggests a potential anti-inflammatory effect (40). This observation is consistent with the alterations in the ω6 to ω3 PUFA ratios in the RPE and neural retina (Fig. S7).

Moreover, a 3-weeks DCF treatment of *AdipoR1*$^{-/-}$ mice resulted in a 19.6% thicker outer nuclear layer ($p < 0.0001$) compared to vehicle-treated mice, demonstrating a protective effect on photoreceptors (Fig. 7, *F* and *G*). We also noticed a general improvement in photopic a-wave amplitudes on electroretinograms, especially at higher light intensity stimulus (30 cd s/m^2), indicating better cone function (Fig. 7*H*). In summary, these results support our hypothesis that inhibiting ceramide production leads to an elevation of PUFA levels, as evidenced by the significant increase in both free and esterified PUFAs in the retina and RPE of *AdipoR1*$^{-/-}$ mice treated with the DCF drug combination.

Discussion

Except for the action of ceramidases, such as AdipoR1, that catalyze the breakdown of ceramides into SPH and free FAs, the relationship between ceramide and PUFA metabolism remains elusive, since PUFAs are seldom found in ceramides (41). Thus, understanding the connection between AdipoR1, ceramides, and PUFAs could offer valuable insights into the pathogenesis of retinal diseases like retinitis pigmentosa (10–12) and AMD (12). We present the first evidence indicating that AdipoR1 plays a pivotal role in maintaining appropriate ω6 to ω3 PUFA balance within the retina and RPE through its regulation of ceramide metabolism. Our findings unveil the critical role of AdipoR1 in the retina's lipid metabolism. As a metabolic gatekeeper, AdipoR1 regulates the conversion of ceramides into free FAs, likely influencing the quantity and variety of PUFAs in the retina. This regulatory role of AdipoR1 underscores its significance in maintaining the delicate balance of ω3 and ω6 PUFAs, which is essential for retinal health. Additionally, by examining the changes in signaling pathways, we documented that AdipoR1 is required for the activity of the PPARα signaling pathway within retinal tissue, in contrast to other non-neuronal tissues like the liver, where AdipoR2 primarily serves as the key activator of PPARα (17).

Moreover, we devised a pharmacological treatment targeting ceramide synthesis, significantly increasing PUFA levels, especially the anti-inflammatory ω3 type. Post-treatment, we evaluated the mice using optical coherence tomography and ERG analyses, finding a positive effect on retinal structure and function. Our findings regarding the role of AdipoR1 in FA metabolism extend the potential for understanding the mechanisms underlying various neurodegenerative and metabolic disorders, including obesity, diabetes, and cardiovascular disease. These observations provide a foundation for future research to identify novel disease targets. However, there is a qualification that the results primarily reflect outcomes from

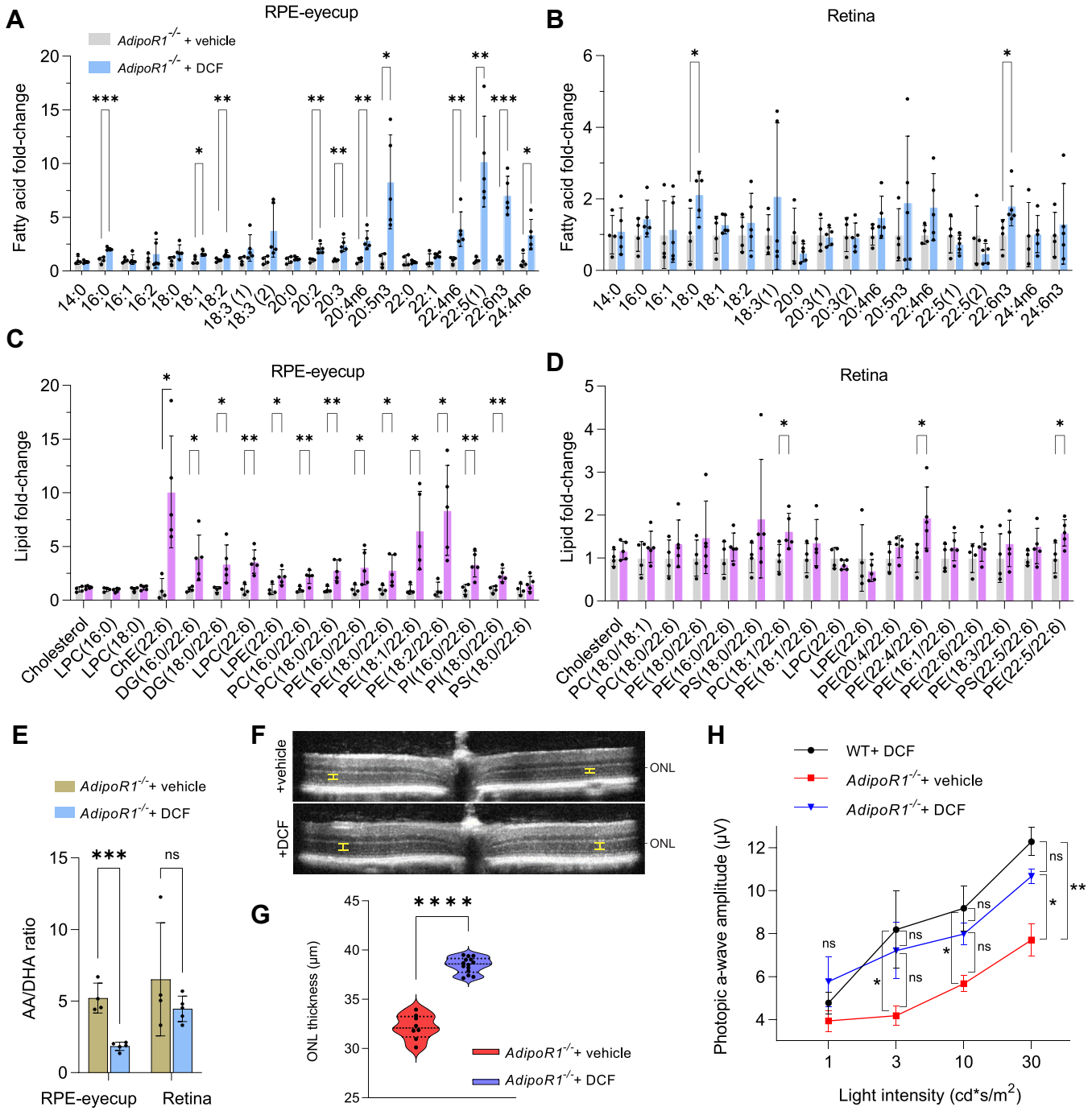

Figure 7. Changes in the lipid levels and improved retina function in *AdipoR1*$^{-/-}$ mice after 3-weeks treatment with ceramide synthesis inhibitors (DCF: desipramine, L-cycloserine, FTY-720). *A–E*, treatment of *AdipoR1*$^{-/-}$ mice with DCF led to changes in the levels of free FAs (*A* and *B*), levels of DHA-containing lipids (*C* and *D*), and the AA/DHA ratio (*E*). *F*, representative optical coherence tomography images of retinas from saline-treated or DCF-treated *AdipoR1*$^{-/-}$ mice after 3-weeks treatment. *Yellow* calipers at the inferior and superior aspects of the section indicate the ONL thickness, measured at 500 μm from the optic nerve head. *G*, the average ONL thickness of both eyes is shown for the control (n = 8) and DCF-treated (n = 14) groups. *H*, ERG recordings of photopic a-wave amplitudes in the WT or *AdipoR1*$^{-/-}$ mice treated with saline or DCF. Data represent the mean ± SD for retinas and RPE-eyecups; n = 5 for *AdipoR1*$^{-/-}$ mice, n = 4 for WT. In (*A–E*, *G*), the statistical significance was determined with a 2-tailed *t* test analysis; and in (*A–D*), the *p*-values were adjusted for multiple comparisons using the Holm–Sidak's correction method: *$P_{adj} < 0.05$, **$P_{adj} < 0.01$, ***$P_{adj} < 0.001$, ****$P_{adj} < 0.0001$. In (*H*), 2-way ANOVA analysis with Tukey post hoc correction for multiple comparisons was used: ns – not significant, *$p < 0.05$, **$p < 0.01$. DHA, docosahexaenoic acid; ERG, electroretinography.

global *AdipoR1*-KO mice, so cell-autonomous effects are not certain. Accordingly, tissue-specific studies are required to clarify the precise role of AdipoR1 in these pathways, particularly within the eye, to develop targeted therapeutic strategies.

AdipoR1 plays a crucial role in PUFA metabolism

We conducted a comprehensive analysis of the lipidome in the retinas, RPE cells, and brains of *AdipoR1*$^{-/-}$ mice while concurrently examining the transcriptome and proteome of the retina and RPE for a holistic understanding of molecular

alterations. This in-depth study revealed significant lipidomic profile differences in the retina, RPE, and brain compared to WT littermates. Notably, the retina and RPE displayed marked changes in lipid composition, while the brain showed minimal alterations. These observations underline the tissue-specific roles of AdipoR1 and AdipoR2 in regulating lipid profiles, with the brain's lipidome being less affected by AdipoR1 deficiency. Interestingly, despite *AdipoR2's* presence in the retina and RPE, its expression was insufficient to counterbalance *AdipoR1* loss, particularly in the retina where its content is lower than that of *AdipoR1* by more than 7-fold. Furthermore, the comparative analysis revealed that *AdipoR2* expression in the RPE is similar to *AdipoR1*, which contrasts sharply with its much lower expression in the retina. This notable difference in *AdipoR2* expression could account for the less pronounced lipidomic changes observed in the RPE compared to the retina. Such findings suggest that while *AdipoR2* may partially compensate for the loss of *AdipoR1* in the RPE, its lower expression in the retina limits its ability to mitigate the impact of *AdipoR1* deficiency.

In the retina of *AdipoR1*$^{-/-}$ mice, we observed a marked increase in certain lipid classes, most importantly sphingolipids such as hexosyl-1-ceramides, SMs, and certain ceramide species, as well as TGs and decrease in others, such as DGs and acylcarnitines. In the RPE, we found increased PE and ChEs and decreased LPC. Furthermore, we observed a substantial shift in the relative abundance of numerous lipid species in these tissues, particularly those containing ω3 PUFAs. We then analyzed the PUFA profile in the retina and RPE of *AdipoR1*$^{-/-}$ mice, revealing a remarkable reduction of up to 99.4% in VLC-PUFAs. This depletion was particularly noticeable in the ω3 family, where species containing six unsaturated bonds ranging from 22:6n3 to 36:6n3 were primarily affected. Despite their otherwise unique lipid profiles, this pattern was consistent across the retina and RPE, suggesting that this is a primary effect related to AdipoR1 ablation in both tissue types. Contrary to the limited scope of previous studies, which reported changes predominantly in specific PUFAs like 22:6n3, 32:6n3, and 32:4n6 (18), our research uncovers a broader spectrum of lipidomic alterations due to AdipoR1 ablation, including significant accumulations of ω6 PUFA species. We observed a substantial increase in several ω6 PUFA species, notably 36:4n6, 34:4n6, 24:4n6, 22:4n6, alongside more modest elevations in 26:4n6 and AA (20:4n6). This pronounced elevation of ω6 PUFAs in *AdipoR1*$^{-/-}$ mice suggests a potential adaptive mechanism, possibly aiming to compensate for the significant reduction in ω3 PUFAs and maintain membrane fluidity, which is essential for optimal photoreceptor function.

Furthermore, we found only a modest reduction in mRNA level and unchanged protein content for ELOVL4, a critical retinal enzyme that produces VLC-PUFAs, consistent with previous observations (18, 20). The unchanged ELOVL4 protein level, coupled with a substantial increase in ω6 VLC-PUFAs (specifically 36:4n6, 34:4n6), suggests that the production and activity of ELOVL4 protein is not repressed upon *AdipoR1* knockout. Moreover, the markedly low levels of ω3 VLC-PUFAs observed could also be a consequence of the reduced availability of ω3 substrates. This ω3 scarcity, coupled with an abundance of ω6 substrates, may lead to ω6 outcompeting ω3 PUFAs at the ELOVL4 enzyme active site (42). Additionally, the intracellular FA-binding protein shuttles, such as FABP7, which was diminished more than −35-fold in the retinas of *AdipoR1*$^{-/-}$ mice, are likely responsible for delivering substrates to ELOVL4. The significant decrease in FABP7, which has a higher affinity for ω3 PUFA, could potentially explain the preferential uptake and elongation of ω6 PUFAs over ω3, impacting the balance of VLC-PUFAs in these tissues. Thus, our omics analyses imply that AdipoR1 plays an important role specifically in regulating the ω3 PUFA transport and elongation rather than those of the ω6 family. Based on this finding, we hypothesize that AdipoR1 might be the first receptor identified to regulate the balance between ω3 and ω6 PUFAs.

Interestingly, this interplay between ω3 and ω6 PUFAs and AdipoR1 is further illuminated by a study where ω3 PUFA supplementation, as opposed to ω6, led to more than a 2-fold increase in *AdipoR1* mRNA levels in a mouse model of retinopathy (25). This finding suggests a potential feedback loop whereby ω3 PUFAs positively regulate *AdipoR1* expression. Such a mechanism would implicate AdipoR1 to be intricately involved in detecting and responding to ω3 PUFA levels in the retina, thereby playing a pivotal role in the dynamic regulation of these essential FAs. While both PUFA types ω6 and ω3 are important for retina development (25), the excess of ω6 PUFAs compared to ω3, observed in pathological conditions such as AdipoR1 ablation, could contribute to chronic inflammation in the retina and other tissues. Hence, the elevation of the ω6/ω3 ratio may be a risk factor in retinal diseases (23–25, 43).

We noted a substantial differential effect on DHA levels in the retinas and RPE cells of the *AdipoR1*$^{-/-}$ mice. The retina exhibited a nearly −2.4-fold decrease in DHA, whereas the RPE showed a 1.9-fold increase, a phenomenon not previously reported (18). The observed discrepancy between our findings and those of the previous study by Rice *et al.* (2015) could be attributed to our more precise approach. Unlike the earlier study, which utilized RPE-eyecups containing a mix of RPE cells, choroid, and sclera, our analysis was conducted exclusively on isolated RPE cells. This methodological refinement provides a more accurate reflection of the FA levels within the RPE cells. Our findings suggest a disrupted DHA transport mechanism from the RPE to the retina in the absence of the AdipoR1 protein despite the increased DHA accumulation in the RPE. Several factors could contribute to the elevated DHA levels in the RPE: (i) enhanced uptake from the choriocapillaris, (ii) increased DHA synthesis within the RPE, (iii) impaired DHA recycling to the photoreceptors *via* phagocytosis in the OSs, (iv) impaired DHA transport from RPE stores, or a combination of these mechanisms (44, 45). However, our findings of contrasting patterns of DHA-containing TGs—decreased in the retina but increased in the RPE—suggest that in *AdipoR1*$^{-/-}$ mice, DHA is accumulated in TGs in the RPE instead of being mobilized to the photoreceptors. This pattern indicates that the RPE cells are not effectively releasing DHA from the TGs for uptake by the photoreceptors.

Moreover, supporting the concept of a disrupted DHA transport mechanism, we noted a significant, nearly 4-fold decrease in the levels of PLIN1 in the retina. PLIN1 serves as a scaffold protein (46) on the surface of LDs, facilitating access of hormone-sensitive lipase to LDs and orchestrating crucial protein–protein interactions essential for efficient lipid mobilization. Consequently, the observed reduction in PLIN1 may indicate compromised liberation of FAs from LDs in the retina.

Additionally, decreased protein levels of FABP7 and FABP5 in the retina and FABP3 in the RPE further suggest disrupted intracellular transport of FAs in the absence of the AdipoR1 protein. In particular, the correlation between diminished levels of FABP7 and reduced DHA content in the retina, compared to the unchanged FABP7 in the RPE with DHA surplus, underscores the crucial role of FABP7 in the intracellular transport of DHA and other ω3 PUFAs. The diminished FABP7 synthesis correlates with the observed DHA deficit in the retina, highlighting the integral role of this protein in DHA transport and indicating a potential mechanistic link to AdipoR1's regulatory function in PUFA metabolism.

AdipoR1's potential role in regulating membrane viscosity

Our lipidomic analysis revealed a notable depletion of ω3 PUFAs with six unsaturated bonds, particularly the VLC variants, while almost all ω6 PUFAs containing four unsaturated bonds displayed an increase. The abundance of double bonds and the resultant "kinked" structure in ω3 PUFAs enhance membrane fluidity by hindering the close packing of FA chains (47–50). Conversely, the fewer double bonds in ω6 PUFAs allow for tighter packing, leading to less fluid cell membranes. Drawing from our lipidomic results and lipid ontology, we discerned an altered lipid profile that may lead to alterations in the mechanical properties and fluidity of the lipid bilayer in the retina of *AdipoR1*$^{-/-}$ mice. Consequently, we propose that AdipoR1 may have a role in influencing membrane fluidity, potentially through regulating the abundance of ω3 PUFAs and controlling their transport and integration into cell membranes. Supporting this interpretation, a study by Ruiz *et al.* reported that the concurrent absence of AdipoR1 and AdipoR2 severely affects fluidity, leading to pathological membrane rigidification (21). Ruiz *et al.* attributed this rigidification to aberrant membrane phospholipids containing excess saturated FAs. Likewise, our analyses indicated increased saturated lipids in the *AdipoR1*$^{-/-}$ retina.

Additionally, there was a marked reduction in polyunsaturated lipids, especially ones containing six unsaturated bonds. These changes can stiffen the membrane, altering the retina's function. Such stiffening would be especially critical for structures like the photoreceptor OS membranes and disks and the proteins involved in the phototransduction cycle, which rely on ample fluidity for optimal performance (51–53).

AdipoR1 and PPARα signaling: implications for PUFA content in the eye

The ceramidase activity of AdipoR1 impacts cell biology in several ways. It regulates ceramide levels, preventing toxic accumulation; it boosts the sphingosine-1-phosphate to ceramide ratio, thereby promoting cell survival; and it generates SPH and free FAs, which act as ligands for the PPAR signaling pathways (7, 9, 14, 21).

In examining the potential role of AdipoR1 in signaling, we postulated that the PPARα signaling pathway, a principal regulator of lipid metabolism influenced by adiponectin receptors, might be responsible for the deficient levels of LC- and VLC-PUFAs in *AdipoR1*$^{-/-}$ mice (54). We hypothesized that the absence of the *AdipoR1* gene in *AdipoR1*$^{-/-}$ mice results in deficient PPARα signaling, leading to reduced PUFA levels in the retina and RPE. To test this hypothesis, we first analyzed RNAseq data from the retina and RPE of *AdipoR1*$^{-/-}$ mice. Our analysis found the PPAR signaling pathway to be one of the significantly enriched terms in the RPE, together with a notable downregulation of the *Ppara* gene in the retina and RPE of *AdipoR1*$^{-/-}$ mice. Additionally, in the RPE, key genes involved in FA transport, namely *Fabp1*, *Slc27a2*, *Slc27a5*, and *Mfsd2a*, which are integral to the PPARα signaling pathway, were significantly reduced. These results indicate a substantial impact of AdipoR1 absence on PPARα signaling and FA transport mechanisms. We then examined whether the proteins with significantly altered expression were associated with specific pathways in the retina and RPE of *AdipoR1*$^{-/-}$ mice. Our protein pathway analysis revealed a downregulation of PPARα signaling in both the retina and RPE, with the latter exhibiting the most pronounced effect. This observation aligned with the RNAseq findings and with our initial hypothesis. Previous studies have emphasized AdipoR1's role as primarily activating the AMPK pathway in the liver and AdipoR2's association with the PPARα pathway (17). Our findings for the retina (part of the CNS) presented a different picture. We did not find significant changes in the AMPK signaling pathway in *AdipoR1*$^{-/-}$ mice; rather, we observed reductions in the PPARα-pathway components at both the mRNA and protein levels.

In the retinal proteome, we noted a significant decrease in the abundance of proteins involved in FA transport, such as FABP7, FABP5, ACSL1, and ACSL6, as well as those involved in FA oxidation, including CPT1A, ACOX1, and a slight reduction of ACADM. FABP7, which displayed the most dramatic decrease of nearly 97%, preferentially binds ω3-PUFAs, such as DHA (55, 56). Consequently, its deficiency could lead to lower levels of this type of PUFA in the retina (55, 56). In the RPE, we observed the most substantial decreases in proteins involved in FA transport, such as CD36, FABP3, ACSL1, and ACSL6, as well as those involved in FA oxidation—ACADL and SCP2. Additionally, we noted a decrease in adiponectin (ADIPOQ), which has recently been proposed as a lipid-transporting protein (57). The observed changes in protein expression related to the transport and oxidation of FAs in both the retina and RPE of *AdipoR1*$^{-/-}$ mice offer intriguing insights into the complex role of AdipoR1 in lipid metabolism within ocular tissues. In the retina, the downregulation of key enzymes such as ACSL1, ACSL6, ACADM, ACOX1, and CPT1A, alongside the upregulation of ACSL3 and PCK2, suggests a profound impact of AdipoR1 deficiency on both the transport and metabolic processing of FAs. ACSL1 and ACSL6 are pivotal in activating LC-FAs, a

crucial step for their subsequent oxidation or incorporation into phospholipids and TGs. The decrease in these enzymes could contribute to an impaired FA transport and activation capacity, potentially leading to an accumulation of unmetabolized FAs or their altered distribution within cellular membranes.

Similarly, the downregulation of ACADM and ACOX1, enzymes involved in β-oxidation of FAs, indicates a diminished capacity for FA catabolism. This diminution could decrease acetyl-CoA generation, a key metabolite in energy production, and may impact the overall energy homeostasis within retinal cells. However, the upregulation of ACSL3 and PCK2 indicates a compensatory or an adaptive response to altered lipid metabolism, with ACSL3 potentially facilitating the production of alternate lipid species and PCK2 enhancing gluconeogenesis, thereby providing an alternative energy source.

In the RPE, similar downregulation patterns were observed for ACSL1, ACSL6, and additional critical proteins such as CD36, ACADL, SCP2, and HMGCS2. The downregulation of CD36, a key FA transporter, suggests impaired lipid uptake from the circulation. Moreover, the decrease in ACADL and SCP2, which are involved in FA oxidation, and HMGCS2, a key enzyme in ketogenesis, further underscores the potential disruption in lipid catabolism and energy provision within the RPE. Such changes could have significant implications for the RPE's ability to support the photoreceptors by recycling visual cycle components and maintaining photoreceptor health.

These alterations in lipid metabolism–related proteins in the retina and RPE highlight the critical role of AdipoR1 in maintaining lipid homeostasis and energy balance within the eye. The deficiency of AdipoR1 appears to disrupt the intricate balance of FA transport, activation, and catabolism, which is essential for the proper functioning of the retina and RPE. This disruption could contribute to the pathophysiology of retinal disease by impairing the supply of FA to photoreceptors, potentially altering membrane composition and fluidity, and reducing the availability of energy substrates. Given the importance of ω3 PUFAs in retinal health, the observed changes could also impact visual function by affecting phototransduction.

Inhibiting ceramide metabolism restores PUFA levels: a novel insight

The study significantly advances our understanding of retinal health by uncovering a previously unexplored relationship between AdipoR1, ceramide metabolism, and the ω6/ω3 PUFA balance. Specifically, through inhibiting ceramide synthesis in AdipoR1-deficient mice using DCF, we effectively boosted PUFA levels in the retina and RPE, with a notable increase in ω3 PUFAs like DHA, eicosapentaenoic acid, and docosapentaenoic acid and improved retina function. This finding is unprecedented and reveals a novel aspect of lipid metabolism regulation within the retina. The observed increase in PUFA levels after inhibition of ceramide synthesis underscores the critical role of AdipoR1 as a ceramidase enzyme. Not only does AdipoR1 facilitate the breakdown of ceramides into SPH and free FA, but it also directly impacts the availability and metabolism of FA. Importantly, the elevated DHA levels were integrated into various lipid structures, including phospholipid species, ChEs, and DGs, indicating a comprehensive restructuring of the lipidome. Incorporating PUFAs into lipids, particularly DHA-containing lipids, suggests a potential mechanism for the improved survival and function of photoreceptors.

In light of our previous findings (9), we note the significant role of ceramide imbalance in contributing to retinal degeneration. Our current study further characterizes this intricate landscape. While ceramide dysregulation is critical in driving photoreceptor apoptosis, it represents only one facet of a multifactorial process. Importantly, our investigations now also elucidate the profound impact of decreased ω3 PUFA production and highlight how diminished PPARα signaling can undermine lipid transport, FA transport, and oxidation processes, consequently leading to ω3 PUFA depletion (58–60). This dual perspective underscores the complexity of the dysregulation mechanisms, where both ceramide accumulation and PUFA depletion contribute to retinal degeneration in AdipoR1 deficiency. Given the intertwined nature of these pathways, it is challenging to delineate their respective contributions precisely. However, our findings suggest that the interplay between ceramide imbalance and ω3 PUFA depletion forms a nexus of metabolic dysregulation that is pivotal in the pathogenesis of retinal diseases associated with AdipoR1 deficiency.

It is also worth noting that, given the systemic nature of the DCF drug administration, the observed correction of PUFA imbalance in the retina and RPE may also be mediated by effects occurring outside the eye. This introduces complexity in determining whether the direct inhibition of ceramide synthesis within the eye would yield comparable results. Our findings show that systemic administration effectively addresses the imbalance within these specific tissues; however, there is potentially a systemic influence on lipid metabolism that benefits the eye indirectly.

Furthermore, our findings reveal an additional layer of intricacy in AdipoR1's functionality. Given the role of ω3 PUFAs as natural ligands for PPARα, our findings suggest a strong link between PUFA regulation by AdipoR1 and the PPARα signaling pathway. This hypothesis warrants further investigation to elucidate the direct effects of AdipoR1 activity on PPARα regulation.

The decrease in the AA to DHA ratio may suggest a potential shift towards an anti-inflammatory state, which could have implications for treating retinal diseases. Several studies (61–63) suggest that lowering the AA/DHA ratio in the retina may be beneficial in various retinal diseases, including AMD, diabetic retinopathy, and retinitis pigmentosa, because of the anti-inflammatory effect of DHA. The protective effect on photoreceptors and the improvement in cone function observed after the ceramide-targeted treatment further support the potential therapeutic benefits of modulating ceramide and PUFA levels in retinal diseases.

Considering its central role in these interconnected metabolic pathways, AdipoR1 emerges as a promising therapeutic

target. Modulating the activity of AdipoR1 might allow us to simultaneously influence ceramide metabolism, PUFA levels, and PPARα signaling. This understanding presents a novel avenue for developing treatment strategies, especially in conditions where lipid imbalances contribute to disease progression.

Implications of AdipoR1 ablation on photoreceptor structure

To evaluate the structural implications of *AdipoR1* knockout, we utilized TEM to assess photoreceptor and RPE morphology. Remarkably, the phenotype of *AdipoR1*$^{-/-}$ mice, displaying alterations in photoreceptor OS structure, mirrors in some ways the effects of loss of the BBS1 or BBS4 proteins, which are associated with BBS, an autosomal recessive ciliopathy (64, 65). These observations suggest an association between AdipoR1 function and ciliary structure or health, warranting further investigation into a potential link between AdipoR1 deficiency and ciliopathies. Remarkably, a patient harboring a homozygous frameshift mutation in *ADIPOR1*, which presumably leads to a total absence of the AdipoR1 protein, exhibited a retinitis pigmentosa-like syndrome along with intellectual impairment and truncal obesity. These manifestations align with the classic symptoms observed in BBS (11). Our findings provide compelling evidence of the crucial role of AdipoR1 in maintaining the structural integrity of the ROSs in photoreceptor cells. The substantial shortening of the ROS and disorganization of the disks in *AdipoR1*$^{-/-}$ mice underscore the importance of this receptor in photoreceptor-cell morphology. Moreover, our proteomic analysis further strengthens this connection, revealing a significant downregulation of proteins related to the photoreceptor OS and the BBSome complex in the retina of *AdipoR1*$^{-/-}$ mice. The BBSome complex, crucial for regulating ciliary trafficking in primary cilia, is known to be disrupted in BBS, leading to retinitis pigmentosa in most affected individuals.

Moreover, we observed a marked downregulation of specific photoreceptor OS proteins, including ABCA4, CNGA-1 (cGMP-gated channel alpha subunit), and ROM1, underscoring the unique sorting mechanisms regulated by AdipoR1. Notably, both ROM1 and the cGMP-gated channel play pivotal roles in OS morphogenesis, and defects in these proteins have been linked to disruptions in OS structure (66, 67). Our results suggest a potential mechanistic link between AdipoR1, the BBSome complex, and ciliary function. These findings provide novel insights into the role of AdipoR1 in photoreceptor cell morphology, with potential implications for a better understanding of retinal disorders.

Conclusions

This study has provided novel insights into the role of AdipoR1, a ceramidase enzyme, in the retina and RPE, specifically focusing on FA and lipid metabolism. Our comprehensive lipidomic, transcriptomic, and proteomic analyses on *AdipoR1*$^{-/-}$ mice revealed distinct alterations in lipid composition, particularly in the retina and RPE. We observed a notable reduction in LC- and VLC-PUFAs, predominantly of the ω3 type, underlining AdipoR1's critical role in sustaining these essential lipids. Furthermore, our findings suggest that AdipoR1 may play a role in the regulation of membrane fluidity by controlling the transport and synthesis of ω3 PUFAs.

Importantly, the downregulation of PPARα signaling in the absence of AdipoR1 indicates a potential mechanistic link between this signaling pathway and PUFA levels in the retina. The administration of ceramide synthesis inhibitors improved retinal function and enhanced ω3 PUFA levels in retina and RPE while reducing the AA/DHA and ω6/ω3 ratios. This suggests a shift towards an anti-inflammatory state, offering a promising therapeutic avenue for retinal diseases.

Collectively, our findings position AdipoR1 as a multifaceted regulator within the retina, crucial not only for lipid metabolism but also for maintaining the structural integrity of the photoreceptors. This expanded understanding of AdipoR1's role highlights its significance in the pathogenesis of retinal diseases and other neurodegenerative conditions, where an imbalance in PUFA levels plays a contributory role (68–70). These insights pave the way for further research, particularly developing targeted therapies that leverage AdipoR1 regulatory functions. Future investigations into the broader implications of AdipoR1 activity, especially in different retinal conditions, are necessary to fully exploit its potential as a therapeutic target.

Experimental procedures

Study approval

All experimental procedures involving mice were approved by the Institutional Animal Care and Use Committee at UCI, Irvine, under Protocol AUP-21-096. These procedures strictly adhered to the Association for Research in Vision and Ophthalmology Statement for the Use of Animals in Ophthalmic and Visual Research. Additionally, the animal experiments with TEM were sanctioned by the Indianapolis Institutional Animal Care and Use Committee. All methodologies employed were consistent with the guidelines of the American Veterinary Medical Association Panel on Euthanasia and the Association for Research in Vision and Ophthalmology.

Mice

The mouse strain used for this research project, B6.129P2-*Adipor1*^{tm1Dgen}/Mmnc, RRID: MMRRC_011599-UNC, was obtained from the Mutant Mouse Resource and Research Center (MMRRC) at the University of North Carolina at Chapel Hill, an NIH-funded strain repository; this strain was donated to the MMRRC by Deltagen. The heterozygous mice were backcrossed into the C57BL/6J and B6(Cg)-*Tyr*$^{c-2J}$/J backgrounds. Homozygous *AdipoR1*$^{-/-}$ mice were created by interbreeding *AdipoR1*$^{+/-}$ mice as described previously (9). Animals were housed under 12 h light/12 h dark cycles and bred using standard procedures. Both male and female mice were used for all experiments.

Desipramine/L-cycloserine treatment

Mice were injected intraperitoneally three times per week (Monday, Wednesday, and Friday) for 3 weeks starting on P15,

either with saline (control group) or with a drug formulation in saline (DCF-treated group) designed to deliver 20 mg/kg desipramine (BML-AR119, Enzo Life Sciences), 100 mg/kg L-cycloserine (AK-87855, Ark Pharm), and 10 mg/kg FTY720 (S5002 Selleck Chemicals) to each mouse (volume adjusted for mouse weight differences). At P36, all mice were examined with optical coherence tomography and ERG. After ERG, under ketamine/xylazine anesthesia, all mice were euthanized by cervical dislocation. The retinas and RPE from both eyes were dissected and used for untargeted lipidomic analysis by LC-MS.

Photopic ERG

Mice were anesthetized with ketamine/xylazine (100/10 mg/kg, i.p.), their pupils were dilated with 1% tropicamide, and then 2.5% hypromellose (Akorn) was applied to keep the corneas hydrated. Two sets of active recording electrodes were placed onto the corneas, and reference and ground electrodes were positioned subcutaneously between the ears and on the tail, respectively. The eyes were stimulated with alternating blue and green light at six different light intensities (0.1, 1, and 10 cd s/m^2 for blue and 0.3, 3, and 30 cd s/m^2 for green). The ERGs were recorded with the Celeris rodent electrophysiology system (Diagnosys LLC) and analyzed with Espion V6 software (Diagnosys LLC, www.diagnosysllc.com). Repeated measures two-way ANOVA followed by Sidak's post hoc test were used for all ERG comparisons.

Transcriptomic analysis

For our transcriptomic analysis, we re-examined bulk RNA-Seq data from the retina and RPE of 1-month AdipoR1−/− and WT mice. This dataset is available in the NCBI Gene Expression Omnibus under the accession number GSE184902. The data was analyzed as described previously (9). We employed EdgeR (v3.20.9) for differential expression analysis, focusing on genes with a log2(fold-change) > 0.585 and false discovery rate (FDR) < 0.05 to identify significantly differentially expressed genes. Differentially expressed genes were subjected to pathway analysis using the KEGG pathway mapping tool (www.kegg.jp/kegg/mapper/) to identify significantly enriched pathways. Gene expressions from the relevant pathways were plotted and subjected to statistical analysis using a 2-tailed *t* test. *p*-values were adjusted using Holm-Sidak's correction method to account for multiple comparisons.

Proteomic analysis

Mice were euthanized by CO_2 inhalation followed by cervical dislocation, and their eyes were enucleated with curved Graefe forceps. After cleaning the globes from fat and muscle tissues and removing the anterior chamber and lens, the neural retina was carefully peeled off the RPE-eyecup. Neural retinas and RPE-eyecups were separately homogenized in UA buffer containing 8 M urea, 0.1 M Tris–HCl (pH 8.5), and a protease inhibitor cocktail (Bimake 14001). The tissue homogenates were sonicated using a 550 sonic dismembrator with a micro tip (Thermo Fisher Scientific). Sonication was performed intermittently on ice, using a cycle of 5 s ON at 30% amplitude followed by a 3-s OFF period for cooling. The total sonication time was 4 min, followed by centrifugation at 12,000*g* for 10 min at 4 °C. The supernatant was collected and digested by the filter-aided sample preparation method. Briefly, the supernatant was transferred into a spin-filter column (30-kDa cutoff). Proteins were reduced with 10 mM DTT for 1 h at 56 °C and alkylated with 20 mM iodoacetic acid for 30 min at RT in the dark. Next, the buffer was changed to 50 mM NH_4HCO_3 by washing the membrane three times. Free trypsin was added to the protein solution at a trypsin:protein ratio of 1:50 and incubated overnight at 37 °C. The tryptic digests were recovered in the supernatant after centrifugation and an additional wash with water. The combined supernatants were vacuum-dried and then adjusted to 200 µl with 0.5% acetic acid. The peptide mixture was then subjected to C18 solid-phase extraction (The Nest Group) for desalting.

Mass spectrometry proteomic data acquisition

Proteomics data were acquired *via* LC-MS/MS using an UltiMate 3000 UHPLC (Thermo Fisher Scientific), coupled in line with an Orbitrap Fusion Lumos mass spectrometer (Thermo Fisher Scientific) with an ESI nanospray source. Mobile phase A composition was 0.1% formic acid in water, and mobile phase B contained 0.1% formic acid in acetonitrile (ACN). Peptides were separated over a 57-min gradient from 4% to 25% buffer B (total run time 90 min per sample) on an Acclaim PepMap RSLC column (50 cm × 75 µm) using a 300 nl/min flow rate. Survey (MS) scans were acquired in Orbitrap (FT) with automated gain control (AGC) target 8E5, maximum injection time 50 ms, and dynamic exclusion of 30 s across the scan range of 375 to 1800 m/z. MS/MS spectra were acquired in data-dependent acquisition mode at top speed for 3 s per cycle; the AGC target was set to 1E4 with a maximum injection time of 35 ms. Ions were subjected to stepped-energy higher-energy collision dissociation fragmentation at a normalized collision energy of 20 ± 5%.

Label-free quantitative analysis

The raw LC-MS/MS data files were analyzed using MaxQuant (v1.5.2.8), with the spectra searched against the UniProt mouse database (updated on May 21st, 2018). The mass tolerances for identification of the peptides were 20 ppm for initial precursor ions and 0.5 Da for fragment ions. Two missed cleavages in tryptic digests were allowed. Cysteine residues were set as static modifications. Oxidation of methionine was set as the variable modification. The peptide identification filter was set at a 1% FDR (*q*).

Integrative proteomics and pathway analysis

After the label-free quantification analysis, proteins that exhibited significant changes (with criteria set at $q < 0.05$ and $|\log_2 FC| \geq 0.585$) were selected for further analysis. The *q*-value used here represents the FDR adjusted *p*-value, which helps control the expected proportion of incorrectly rejected null hypotheses. The adjustment used the Benjamini, Krieger,

and Yekutieli correction, an FDR-based method. The significantly changed proteins underwent STRING analysis using the platform available at https://string-db.org (v11.5) for protein–protein interaction networks and functional enrichment analysis. KEGG pathway analysis was employed to determine the functional pathways associated with these significantly altered proteins, utilizing the KEGG database.

Lipidomic analysis

Mice were euthanized by CO_2 inhalation followed by cervical dislocation, and their eyes were enucleated with curved Graefe forceps. After cleaning the globes from fat and muscle tissues and removing the anterior chamber and lens, the neural retina was carefully peeled off the RPE-eyecup. To isolate RPE cells, 200 µl of 1x PBS buffer was added to the RPE-eyecup, and the tube was vigorously tapped for 1 min, followed by flushing the RPE-eyecup with PBS buffer using a 200 µl pipette. The remaining choroid-sclera was removed from the tube, and RPE cells were pelleted by centrifugation at 500 RCF for 5 min at 4 °C. Tissues were frozen in dry ice and stored at −80 °C until subsequent analysis.

Lipid extractions were performed according to the methodology of Bligh and Dyer (71). In brief, 10 µl of the internal standard, Splash Lipidomix Mass Spec Standard (suspended in 1000 µl) (330707, Avanti Polar Lipids), was added to each sample. Then, the tissue was homogenized in 200 µl water, transferred to a glass vial, and 750 µl 1:2 (v/v) $CHCl_3$: MeOH was added and mixed well *via* vortexing. Then 250 µl $CHCl_3$ was added and mixed well. Finally, 250 µl of double-distilled H_2O was added and mixed well. The samples were centrifuged at 3000 RPM for 5 min at 4 °C. The lower phase was transferred to a new glass vial, dried under nitrogen, and stored at −20 °C until subsequent lipid analysis.

LC-MS/MS

Lipids were separated on an Accucore C30 column (2.6 µm, 2.1 mm × 150 mm, Thermo Fisher Scientific). The column-oven temperature was 45 °C. Binary gradient elution was carried out using different ratios of eluents A (ACN:water, 60:40,v/v) and B (IPA:ACN, 90:10, v/v), both containing 10 mM ammonium formate and 0.1% formic acid and the following gradient: −3 to 0 min isocratic elution with 30% B for the equilibration of the column; 0 to 2 min, 30–43% B; 2 to 2.1 min, 43 to 55%; 2.1 to 12 min, 55 to 65% B; 12 to 18 min, 65–85% B; 18 to 20 min, 85–100% B; 20 to 25 min, 100% B; 25 to 25.1 min, 100 - 30%; 25.1 to 28 min, 30% B for column washing and equilibration. The flow rate was set to 260 µl/min, and the temperature of the sample tray was set at 10 °C. The Q-Exactive MS was operated in a full MS-scan mode (resolution 70,000 at m/z 200) followed by data-dependent MS2 (ddMS2) (17,500 resolution) in positive and negative modes. The AGC target value was set at 1E6 or 1E5 for the MS or MS/MS scans, respectively. The maximum injection time was 200 ms for MS and 50 ms for MS/MS. HCD was performed with a stepped-collision energy of 30 ± 10% for negative-ion mode and 25% - 30% for positive-ion mode, with an isolation window of 1.5 Da.

Lipidomic data analysis

Data were analyzed with LipidSearch software (v4.2.21; www.thermofisher.com). Only peaks with molecular identification grade A or B were accepted (A: lipid class and FA completely identified; or B: lipid class and some FA identified). Data visualization was performed on Prism 7 software (GraphPad, www.graphpad.com). To classify significantly dysregulated lipids, an enrichment analysis was conducted using the web application (LION/web) (www.lipidontology.com) (72). Enrichment analysis of lipid ontology terms (LION) was performed on normalized data from LipidSearch. The "ranking mode" with one-tailed *t* test values as local statistics was employed.

Analysis of PUFAs by LC-MS

One microgram of 6Z,9Z,12Z,15Z,18Z-heneicosapentaenoic acid (FA 21:5, Cayman) was added as internal standard. Lipids were extracted by the Bligh-Dyer method, followed by hydrolysis and extraction of total FAs as described in (73). Briefly, 720 µl acetonitrile and 10 µl hydrochloric acid were added to the dried film, and the sample was kept at 95 °C for 1 h. Then, 1 ml of hexane was added to the sample and mixed. The upper phase containing total FAs was transferred to a new tube and evaporated under nitrogen. For further LC-MS analysis, the total FAs were dissolved in acetonitrile-isopropanol (50/50, v/v). Separation of LC- and VLC-PUFAs was achieved on an Acquity UPLC BEH C18 column (1.7 µm, 2.1 mm × 100 mm, Waters Corporation), using a mobile phase consisting of (A) 1% ammonium acetate (1 mol/L) and 0.1% formic acid in water and (B) acetonitrile/isopropanol (1/1, v/v), 1% ammonium acetate (1 mol/L), and 0.1% formic acid, at a flow rate of 0.4 ml/min, with the following linear gradient: 0 to 2 min: 35% −80% B; 2 to 7 min: 80 to 100% B; 7 to 14 min: 100% B; 14 to 15 min: 100-35% B. For quantification, the Q-Exactive MS (Thermo Fisher Scientific) was operated in a full MS-scan mode (resolution 70,000) in negative-ion mode with a scan range of m/z 250–800. Then the VLC-PUFAs of interest were quantified by extracting a chromatographic peak for the corresponding $[M\text{-}H]^-$ ions, using 5 ppm tolerance. The comparison was made by normalizing each peak area with the internal standard FA 21:5 and tissue weight.

Transmission electron microscopy

Eyeballs from albino *AdipoR1*$^{-/-}$ mice and albino B6 WT mice (strain 000058, The Jackson Laboratory) approximately 1-month (PND 31–38; n = 2 for each genotype) were collected post-euthanasia and dissected in PBS (136.9 mM NaCl, 2.7 mM KCl, 8.1 mM Na_2HPO_4, 1.5 mM KH_2PO_4). The resulting eye cups were processed as described previously (74) with the following modifications. The eye cups were fixed with 2% paraformaldehyde, 2.5% glutaraldehyde, 31.3 mM NaH_2PO_4, 23.2 mM NaOH, 2.5% DMSO, 0.022 mM $CaCl_2$, 0.026 mM $MgCl_2$ for 2 to 3 h at RT. During the fixation, the

eye cups were hemisected. They were further fixed for 2 h at 33 to 37 °C. Plastic blocks were sectioned with an ultramicrotome (UCT Ultracut, Leica Biosystems). Thin sections (80–90 nm) were mounted on 50 mesh grids (G50-Ni, Electron Microscopy Sciences) coated with formvar film. After drying, sections were stained with saturated uranyl acetate (∼8%) in 50% ethanol for 10 min at RT, then rinsed with 50% ethanol. Ultrastructures of photoreceptor and RPE cells were observed with a Tecnai Spirit transmission electron microscope (Thermo Fisher Scientific) at 80 kV at the Indiana University School of Medicine Center for Electron Microscopy.

Retinal cross-sections

Mice were euthanized by CO_2 inhalation followed by cervical dislocation. Eyes were enucleated and rinsed briefly with PBS. Using a 23G needle, two small punctures were made in each eyeball at the junction of the cornea and sclera, and the eyes were fixed in PBS-buffered 4% paraformaldehyde for 15 min. The cornea was cut off, followed by removal of the lens and vitreous, and the eyecup was further fixed for 15 min. Next, the eyecup was gently washed three times in PBS for 5 min and transferred to a sucrose solution in PBS (10% and 20% sucrose for 30 min each at room temperature, then 30% sucrose overnight at 4 °C). The next day, the eyecup was embedded in O.C.T. (Tissue-Tek) and snap-frozen in liquid nitrogen vapor. The eyecup was cut into 8-μm-thick serial sections using a cryostat and stored at −80 °C.

ORO staining

ORO solution was freshly prepared before the experiment. A saturated (∼1%) stock solution of ORO (O0625, Millipore Sigma) in 99.9% isopropanol was mixed with water in a 3:2 ratio. Next, the ORO solution was swirled briefly, filtered through a 0.22-μm Steriflip-GP Filter Unit (SCGP00525, Millipore Sigma), and used for tissue staining. Frozen retina cross-sections were thawed and stained for 12 min, rinsed briefly in 60% isopropanol, then in water. Nuclei were counterstained for 3 min in hematoxylin (VWR, 95057-844) and dipped several times in water. Sections were dried briefly and mounted in mounting medium (H-1000, Vector Labs).

Lipid extraction and LC-MS analysis after treatment

The data shown in Figure 7, *A–E* were generated at the MS Core at the Salk Institute. Lipids were extracted using a modified version of the Bligh-Dyer method (71). Briefly, tissue samples were homogenized in 1 ml of PBS using a Microson Ultrasonic Cell Disruptor (model XL-2000) from Misonix. The tissues underwent a sequence of a 10-s sonication pulse, then a 30-s rest on ice, repeated four times. The device power level was adjusted to 6. Samples were transferred to a glass vial (VWR), mixed with 1 ml methanol and 2 ml chloroform containing internal standards (^{13}C16-palmitic acid, d^7-cholesterol), and shaken for 30 s. The resulting mixture was further mixed for 15 s and centrifuged at 2400*g* for 6 min to induce phase separation. The organic (bottom) layer was retrieved using a Pasteur pipette, dried under a gentle stream of nitrogen, and reconstituted in 2:1 chloroform: methanol for LC-MS analysis. Lipidomic analysis was performed on a Vanquish HPLC-online with a Q-Exactive quadrupole-orbitrap mass spectrometer, equipped with an electrospray ion source (Thermo Fisher Scientific). Data were acquired in positive- and negative-ionization modes. Solvent A comprised 95:5 water:methanol; solvent B was 60:35:5 isopropanol:methanol:water. For the positive mode, solvents A and B contained 5 mM ammonium formate with 0.1% formic acid; for the negative mode, solvents contained 0.028% ammonium hydroxide. A Bio-Bond (Dikma) C4 column (5 μm, 4.6 mm × 50 mm) was used. The gradient was held at 0% B between 0 and 5 min, raised to 20% B at 5.1 min, increased linearly from 20% to 100% B between 5.1 and 55 min, held at 100% B between 55 min and 63 min, returned to 0% B at 63.1 min, and held at 0% B until 70 min. The flow rate was 0.1 ml/min from 0 to 5 min, 0.4 ml/min between 5.1 and 55 min, and 0.5 ml/min between 55 and 70 min. The spray voltage was 3.5 kV or 2.5 kV for positive- or negative-ionization modes, respectively. Sheath, auxiliary, and sweep gases were 53, 14, and 3 units, respectively. The capillary temperature was 275 °C. Data were collected in full MS/ddMS2 mode (top 5). Full MS was acquired from 150 to 1500 m/z with a resolution of 70,000, AGC target of 1×10^6, and a maximum injection time of 100 ms. MS2 was acquired with a resolution of 17,500, a fixed first mass of 50 m/z, an AGC target of 1×10^5, and a maximum injection time of 200 ms. Stepped normalized-collision energies were 20, 30, and 40%. Lipid identification was performed with LipidSearch (Thermo Fisher Scientific). Mass accuracy, chromatography, and peak integration of all identified lipids were verified with Skyline (75). Skyline peak areas were used in data reporting, and data were normalized using internal standards and the protein content of the sample.

Data availability

The mass spectrometry proteomics data have been deposited to the ProteomeXchange Consortium *via* the PRIDE (76) repository with the dataset identifier PXD050916.

Supporting information—This article contains supporting information.

Acknowledgments—We thank Yilu Xie from the Department of Ophthalmology at UCI for assistance with histology. The authors acknowledge support to the Gavin Herbert Eye Institute at the University of California, Irvine, from an unrestricted grant from Research to Prevent Blindness and from NIH core grant P30 EY034070 and Department of Ophthalmology, Indiana University School of Medicine from Research to Prevent Blindness (Challenge Grant).

Author contributions—D. L. and K. P. conceptualization; D. L., F. G., S. I., A. T., M. B., Z. D., A. F. M. P., M. T., Y. I., and K. P. data curation; D. L., F. G., S. I., and Y. I. visualization; D. L., Y. I., D. S.-K., and K. P. writing–original draft; D. L., F. G., S. I., A. T., M. B., Z. D.,

A. F. M. P., M. T., P. D. K., Y. I., D. S.-K., and K. P. writing–review and editing; D. L. and K. P. supervision; D. L., F. G., S. I., A. T., and M. B. validation; D. L., F. G., S. I., A. T., M. B., Z. D., A. F. M. P., M. T., P. D. K., Y. I., and D. S.-K. formal analysis; D. L., F. G., S. I., A. T., M. B., Z. D., A. F. M. P., M. T., P. D. K., Y. I., D. S.-K., and K. P. investigation; D. L., F. G., S. I., M. T., Y. I., and K. P. methodology; K. P. funding acquisition; K. P. project administration; K. P. resources.

Funding and additional information—This research was supported in part by grants to: D. L., A. T., and M. B. from Knights Templar Eye Foundation; D. L. from Gavin Herbert Eye Institute Society 20/20; A. F. M. P. from NIH (1S10OD021815-01); M. T. through the International Centre for Translational Eye Research grant (MAB/2019/12) within the International Research Agendas program of the Foundation for Polish Science, co-financed by the EU under the European Regional Development Fund; P. D. K. from the Department of Veterans Affairs (I01BX004939); Y. I. from NEI (R01EY029680 and R01EY028884); D. S.-K. from The Edward N. & Della L. Thome Memorial Foundation Award Program in AMD Research; K. P. from NEI (EY034501 and EY030873). The content is solely the responsibility of the authors and does not necessarily represent the official views of the National Institutes of Health.

Conflict of interest—K. P. is a consultant for Polgenix Inc and serves on the Scientific Advisory Board at Hyperion Eye Ltd. D. S.-K. is a scientific consultant for Visgenx, Inc. All other authors declare that they have no conflict of interests with the contents of this article.

Abbreviations—The abbreviations used are: AA, arachidonic acid; AcCa, acylcarnitine; ACN, acetonitrile; AGC, automated gain control; AMD, age-related macular degeneration; BBS, Bardet-Biedl syndrome; ChE, cholesterol ester; DG, diglyceride; DHA, docosahexaenoic acid; ERG, electroretinography; KEGG, Kyoto Encyclopedia of Genes and Genomes; LC, long chain; LO, lipid ontology; LPC, lyso-phosphatidylcholine; LPE, lyso-phosphatidylethanolamine; MMRRC, Mutant Mouse Resource and Research Center; ORO, Oil Red O; OS, outer segment; PC, phosphatidylcholine; PE, phosphatidylethanolamine; PUFA, polyunsaturated fatty acid; ROM1, ROS membrane protein 1; ROS, rod outer segment; RPE, retinal pigmented epithelium; SM, sphingomyelin; SPH, sphingosine; TEM, transmission electron microscopy; TG, triglyceride; VLC, very long chain.

References

1. SanGiovanni, J. P., and Chew, E. Y. (2005) The role of omega-3 long-chain polyunsaturated fatty acids in health and disease of the retina. *Prog. Retin. Eye Res.* **24**, 87–138
2. Nwagbo, U., and Bernstein, P. S. (2023) Understanding the roles of very-long-chain polyunsaturated fatty acids (VLC-PUFAs) in eye health. *Nutrients* **15**, 3096
3. Jun, B., Mukherjee, P. K., Asatryan, A., Kautzmann, M. A., Heap, J., Gordon, W. C., *et al.* (2017) Elovanoids are novel cell-specific lipid mediators necessary for neuroprotective signaling for photoreceptor cell integrity. *Sci. Rep.* **7**, 5279
4. Bazan, N. G., Molina, M. F., and Gordon, W. C. (2011) Docosahexaenoic acid signalolipidomics in nutrition: significance in aging, neuroinflammation, macular degeneration, Alzheimer's, and other neurodegenerative diseases. *Annu. Rev. Nutr.* **31**, 321–351
5. Orban, T., Johnson, W. M., Dong, Z., Maeda, T., Maeda, A., Sakai, T., *et al.* (2015) Serum levels of lipid metabolites in age-related macular degeneration. *FASEB J.* **29**, 4579–4588
6. Eynard, A. R., and Repossi, G. (2019) Role of omega3 polyunsaturated fatty acids in diabetic retinopathy: a morphological and metabolically cross talk among blood retina barriers damage, autoimmunity and chronic inflammation. *Lipids Health Dis.* **18**, 114
7. Vasiliauskaite-Brooks, I., Sounier, R., Rochaix, P., Bellot, G., Fortier, M., Hoh, F., *et al.* (2017) Structural insights into adiponectin receptors suggest ceramidase activity. *Nature* **544**, 120–123
8. Yamauchi, T., Kamon, J., Ito, Y., Tsuchida, A., Yokomizo, T., Kita, S., *et al.* (2003) Cloning of adiponectin receptors that mediate antidiabetic metabolic effects. *Nature* **423**, 762–769
9. Lewandowski, D., Foik, A. T., Smidak, R., Choi, E. H., Zhang, J., Hoang, T., *et al.* (2022) Inhibition of ceramide accumulation in AdipoR1-/- mice increases photoreceptor survival and improves vision. *JCI Insight* **7**, e156301
10. Zhang, J., Wang, C., Shen, Y., Chen, N., Wang, L., Liang, L., *et al.* (2016) A mutation in ADIPOR1 causes nonsyndromic autosomal dominant retinitis pigmentosa. *Hum. Genet.* **135**, 1375–1387
11. Xu, M., Eblimit, A., Wang, J., Li, J., Wang, F., Zhao, L., *et al.* (2016) ADIPOR1 is mutated in syndromic retinitis pigmentosa. *Hum. Mutat.* **37**, 246–249
12. Kaarniranta, K., Paananen, J., Nevalainen, T., Sorri, I., Seitsonen, S., Immonen, I., *et al.* (2012) Adiponectin receptor 1 gene (ADIPOR1) variant is associated with advanced age-related macular degeneration in Finnish population. *Neurosci. Lett.* **513**, 233–237
13. Nguyen, L. N., Ma, D., Shui, G., Wong, P., Cazenave-Gassiot, A., Zhang, X., *et al.* (2014) Mfsd2a is a transporter for the essential omega-3 fatty acid docosahexaenoic acid. *Nature* **509**, 503–506
14. Lewandowski, D., Sander, C. L., Tworak, A., Gao, F., Xu, Q., and Skowronska-Krawczyk, D. (2022) Dynamic lipid turnover in photoreceptors and retinal pigment epithelium throughout life. *Prog. Retin. Eye Res.* **89**, 101037
15. Christofides, A., Konstantinidou, E., Jani, C., and Boussiotis, V. A. (2021) The role of peroxisome proliferator-activated receptors (PPAR) in immune responses. *Metabolism* **114**, 154338
16. Vamecq, J., and Latruffe, N. (1999) Medical significance of peroxisome proliferator-activated receptors. *Lancet* **354**, 141–148
17. Yamauchi, T., Nio, Y., Maki, T., Kobayashi, M., Takazawa, T., Iwabu, M., *et al.* (2007) Targeted disruption of AdipoR1 and AdipoR2 causes abrogation of adiponectin binding and metabolic actions. *Nat. Med.* **13**, 332–339
18. Rice, D. S., Calandria, J. M., Gordon, W. C., Jun, B., Zhou, Y., Gelfman, C. M., *et al.* (2015) Adiponectin receptor 1 conserves docosahexaenoic acid and promotes photoreceptor cell survival. *Nat. Commun.* **6**, 6228
19. Sluch, V. M., Banks, A., Li, H., Crowley, M. A., Davis, V., Xiang, C., *et al.* (2018) ADIPOR1 is essential for vision and its RPE expression is lost in the Mfrp(rd6) mouse. *Sci. Rep.* **8**, 14339
20. Osada, H., Toda, E., Homma, K., Guzman, N. A., Nagai, N., Ogawa, M., *et al.* (2021) ADIPOR1 deficiency-induced suppression of retinal ELOVL2 and docosahexaenoic acid levels during photoreceptor degeneration and visual loss. *Cell Death Dis.* **12**, 458
21. Ruiz, M., Devkota, R., Panagaki, D., Bergh, P. O., Kaper, D., Henricsson, M., *et al.* (2022) Sphingosine 1-phosphate mediates adiponectin receptor signaling essential for lipid homeostasis and embryogenesis. *Nat. Commun.* **13**, 7162
22. Patel, S. A., Hoehn, K. L., Lawrence, R. T., Sawbridge, L., Talbot, N. A., Tomsig, J. L., *et al.* (2012) Overexpression of the adiponectin receptor AdipoR1 in rat skeletal muscle amplifies local insulin sensitivity. *Endocrinology* **153**, 5231–5246
23. Gorusupudi, A., Liu, A., Hageman, G. S., and Bernstein, P. S. (2016) Associations of human retinal very long-chain polyunsaturated fatty acids with dietary lipid biomarkers. *J. Lipid Res.* **57**, 499–508
24. Kalogerou, M., Ioannou, S., Kolovos, P., Prokopiou, E., Potamiti, L., Kyriacou, K., *et al.* (2022) Omega-3 fatty acids promote neuroprotection, decreased apoptosis and reduced glial cell activation in the retina of a mouse model of OPA1-related autosomal dominant optic atrophy. *Exp. Eye Res.* **215**, 108901
25. Fu, Z., Yan, W., Chen, C. T., Nilsson, A. K., Bull, E., Allen, W., *et al.* (2022) Omega-3/Omega-6 long-chain fatty acid imbalance in phase I retinopathy of Prematurity. *Nutrients* **14**, 1333

26. Imanishi, Y., Batten, M. L., Piston, D. W., Baehr, W., and Palczewski, K. (2004) Noninvasive two-photon imaging reveals retinyl ester storage structures in the eye. *J. Cell Biol.* **164**, 373–383
27. Imanishi, Y., Gerke, V., and Palczewski, K. (2004) Retinosomes: new insights into intracellular managing of hydrophobic substances in lipid bodies. *J. Cell Biol.* **166**, 447–453
28. Tauchi-Sato, K., Ozeki, S., Houjou, T., Taguchi, R., and Fujimoto, T. (2002) The surface of lipid droplets is a phospholipid monolayer with a unique Fatty Acid composition. *J. Biol. Chem.* **277**, 44507–44512
29. Orban, T., Palczewska, G., and Palczewski, K. (2011) Retinyl ester storage particles (retinosomes) from the retinal pigmented epithelium resemble lipid droplets in other tissues. *J. Biol. Chem.* **286**, 17248–17258
30. Mihalik, S. J., Steinberg, S. J., Pei, Z., Park, J., Kim, D. G., Heinzer, A. K., *et al.* (2002) Participation of two members of the very long-chain acyl-CoA synthetase family in bile acid synthesis and recycling. *J. Biol. Chem.* **277**, 24771–24779
31. Falcon, A., Doege, H., Fluitt, A., Tsang, B., Watson, N., Kay, M. A., *et al.* (2010) FATP2 is a hepatic fatty acid transporter and peroxisomal very long-chain acyl-CoA synthetase. *Am. J. Physiol. Endocrinol. Metab.* **299**, E384–E393
32. Wong, B. H., Chan, J. P., Cazenave-Gassiot, A., Poh, R. W., Foo, J. C., Galam, D. L., *et al.* (2016) Mfsd2a is a transporter for the essential omega-3 fatty acid docosahexaenoic acid (DHA) in eye and is important for photoreceptor cell development. *J. Biol. Chem.* **291**, 10501–10514
33. Lobanova, E. S., Schuhmann, K., Finkelstein, S., Lewis, T. R., Cady, M. A., Hao, Y., *et al.* (2019) Disrupted blood-retina Lysophosphatidylcholine transport impairs photoreceptor health but not visual signal Transduction. *J. Neurosci.* **39**, 9689–9701
34. Paton, C. M., and Ntambi, J. M. (2009) Biochemical and physiological function of stearoyl-CoA desaturase. *Am. J. Physiol. Endocrinol. Metab.* **297**, E28–E37
35. Szklarczyk, D., Gable, A. L., Lyon, D., Junge, A., Wyder, S., Huerta-Cepas, J., *et al.* (2019) STRING v11: protein-protein association networks with increased coverage, supporting functional discovery in genome-wide experimental datasets. *Nucleic Acids Res.* **47**, D607–D613
36. Hsu, Y., Garrison, J. E., Kim, G., Schmitz, A. R., Searby, C. C., Zhang, Q., *et al.* (2017) BBSome function is required for both the morphogenesis and maintenance of the photoreceptor outer segment. *PLoS Genet.* **13**, e1007057
37. Forsythe, E., and Beales, P. L. (2013) Bardet-Biedl syndrome. *Eur. J. Hum. Genet.* **21**, 8–13
38. Hjortshoj, T. D., Gronskov, K., Brondum-Nielsen, K., and Rosenberg, T. (2009) A novel founder BBS1 mutation explains a unique high prevalence of Bardet-Biedl syndrome in the Faroe Islands. *Br. J. Ophthalmol.* **93**, 409–413
39. Castro-Sanchez, S., Alvarez-Satta, M., Corton, M., Guillen, E., Ayuso, C., and Valverde, D. (2015) Exploring genotype-phenotype relationships in Bardet-Biedl syndrome families. *J. Med. Genet.* **52**, 503–513
40. Calder, P. C. (2009) Polyunsaturated fatty acids and inflammatory processes: new twists in an old tale. *Biochimie* **91**, 791–795
41. Furland, N. E., Oresti, G. M., Antollini, S. S., Venturino, A., Maldonado, E. N., and Aveldano, M. I. (2007) Very long-chain polyunsaturated fatty acids are the major acyl groups of sphingomyelins and ceramides in the head of mammalian spermatozoa. *J. Biol. Chem.* **282**, 18151–18161
42. Tu, W. C., Cook-Johnson, R. J., James, M. J., Muhlhausler, B. S., and Gibson, R. A. (2010) Omega-3 long chain fatty acid synthesis is regulated more by substrate levels than gene expression. *Prostaglandins Leukot. Essent. Fatty Acids* **83**, 61–68
43. DiNicolantonio, J. J., and J, O. K. (2019) Importance of maintaining a low omega-6/omega-3 ratio for reducing platelet aggregation, coagulation and thrombosis. *Open Heart* **6**, e001011
44. Gordon, W. C., Rodriguez de Turco, E. B., and Bazan, N. G. (1992) Retinal pigment epithelial cells play a central role in the conservation of docosahexaenoic acid by photoreceptor cells after shedding and phagocytosis. *Curr. Eye Res.* **11**, 73–83
45. Rodriguez de Turco, E. B., Parkins, N., Ershov, A. V., and Bazan, N. G. (1999) Selective retinal pigment epithelial cell lipid metabolism and remodeling conserves photoreceptor docosahexaenoic acid following phagocytosis. *J. Neurosci. Res.* **57**, 479–486
46. Brasaemle, D. L., Subramanian, V., Garcia, A., Marcinkiewicz, A., and Rothenberg, A. (2009) Perilipin A and the control of triacylglycerol metabolism. *Mol. Cell. Biochem.* **326**, 15–21
47. Harayama, T., and Shimizu, T. (2020) Roles of polyunsaturated fatty acids, from mediators to membranes. *J. Lipid Res.* **61**, 1150–1160
48. Leekumjorn, S., Cho, H. J., Wu, Y., Wright, N. T., Sum, A. K., and Chan, C. (2009) The role of fatty acid unsaturation in minimizing biophysical changes on the structure and local effects of bilayer membranes. *Biochim. Biophys. Acta* **1788**, 1508–1516
49. Yang, X., Sheng, W., Sun, G. Y., and Lee, J. C. (2011) Effects of fatty acid unsaturation numbers on membrane fluidity and alpha-secretase-dependent amyloid precursor protein processing. *Neurochem. Int.* **58**, 321–329
50. Hashimoto, M., Hossain, S., Yamasaki, H., Yazawa, K., and Masumura, S. (1999) Effects of eicosapentaenoic acid and docosahexaenoic acid on plasma membrane fluidity of aortic endothelial cells. *Lipids* **34**, 1297–1304
51. Boesze-Battaglia, K., Damek-Poprawa, M., Mitchell, D. C., Greeley, L., Brush, R. S., Anderson, R. E., *et al.* (2008) Alteration of retinal rod outer segment membrane fluidity in a rat model of Smith-Lemli-Opitz syndrome. *J. Lipid Res.* **49**, 1488–1499
52. Potvin-Fournier, K., Valois-Paillard, G., Lefevre, T., Cantin, L., Salesse, C., and Auger, M. (2017) Membrane fluidity is a driving force for recoverin myristoyl immobilization in zwitterionic lipids. *Biochem. Biophys. Res. Commun.* **490**, 1268–1273
53. Litman, B. J., and Mitchell, D. C. (1996) A role for phospholipid polyunsaturation in modulating membrane protein function. *Lipids* **31**, S193–S197
54. Sharma, A., Mah, M., Ritchie, R. H., and De Blasio, M. J. (2022) The adiponectin signalling pathway - a therapeutic target for the cardiac complications of type 2 diabetes? *Pharmacol. Ther.* **232**, 108008
55. Balendiran, G. K., Schnutgen, F., Scapin, G., Borchers, T., Xhong, N., Lim, K., *et al.* (2000) Crystal structure and thermodynamic analysis of human brain fatty acid-binding protein. *J. Biol. Chem.* **275**, 27045–27054
56. Xu, L. Z., Sanchez, R., Sali, A., and Heintz, N. (1996) Ligand specificity of brain lipid-binding protein. *J. Biol. Chem.* **271**, 24711–24719
57. Ye, J. J., Bian, X., Lim, J., and Medzhitov, R. (2020) Adiponectin and related C1q/TNF-related proteins bind selectively to anionic phospholipids and sphingolipids. *Proc. Natl. Acad. Sci. U. S. A.* **117**, 17381–17388
58. Leone, T. C., Weinheimer, C. J., and Kelly, D. P. (1999) A critical role for the peroxisome proliferator-activated receptor (PPAR) in the cellular fasting response:: the PPAR -null mouse as a model of fatty acid oxidation disorders. *Proc. Natl. Acad. Sci. U. S. A.* **96**, 7473–7478
59. Zeng, W., Yin, X., Jiang, Y., Jin, L., and Liang, W. (2022) PPARalpha at the crossroad of metabolic-immune regulation in cancer. *FEBS J.* **289**, 7726–7739
60. Bougarne, N., Weyers, B., Desmet, S. J., Deckers, J., Ray, D. W., Staels, B., *et al.* (2018) Molecular actions of PPARalpha in lipid metabolism and inflammation. *Endocr. Rev.* **39**, 760–802
61. Tuo, J., Ross, R. J., Herzlich, A. A., Shen, D., Ding, X., Zhou, M., *et al.* (2009) A high omega-3 fatty acid diet reduces retinal lesions in a murine model of macular degeneration. *Am. J. Pathol.* **175**, 799–807
62. Chen, W., Esselman, W. J., Jump, D. B., and Busik, J. V. (2005) Anti-inflammatory effect of docosahexaenoic acid on cytokine-induced adhesion molecule expression in human retinal vascular endothelial cells. *Invest. Ophthalmol. Vis. Sci.* **46**, 4342–4347
63. Bazan, N. G. (2006) Cell survival matters: docosahexaenoic acid signaling, neuroprotection and photoreceptors. *Trends Neurosci.* **29**, 263–271
64. Masek, M., Etard, C., Hofmann, C., Hulsmeier, A. J., Zang, J., Takamiya, M., *et al.* (2022) Loss of the Bardet-Biedl protein Bbs1 alters photoreceptor outer segment protein and lipid composition. *Nat. Commun.* **13**, 1282
65. Mykytyn, K., Mullins, R. F., Andrews, M., Chiang, A. P., Swiderski, R. E., Yang, B., *et al.* (2004) Bardet-Biedl syndrome type 4 (BBS4)-null mice implicate Bbs4 in flagella formation but not global cilia assembly. *Proc. Natl. Acad. Sci. U. S. A.* **101**, 8664–8669

66. Clarke, G., Goldberg, A. F., Vidgen, D., Collins, L., Ploder, L., Schwarz, L., *et al.* (2000) Rom-1 is required for rod photoreceptor viability and the regulation of disk morphogenesis. *Nat. Genet.* **25**, 67–73
67. Zhang, Y., Molday, L. L., Molday, R. S., Sarfare, S. S., Woodruff, M. L., Fain, G. L., *et al.* (2009) Knockout of GARPs and the beta-subunit of the rod cGMP-gated channel disrupts disk morphogenesis and rod outer segment structural integrity. *J. Cell Sci.* **122**, 1192–1200
68. Bazinet, R. P., and Laye, S. (2014) Polyunsaturated fatty acids and their metabolites in brain function and disease. *Nat. Rev. Neurosci.* **15**, 771–785
69. Mesa-Herrera, F., Taoro-Gonzalez, L., Valdes-Baizabal, C., Diaz, M., and Marin, R. (2019) Lipid and lipid Raft alteration in aging and neurodegenerative diseases: a window for the development of new biomarkers. *Int. J. Mol. Sci.* **20**, 3810
70. Laye, S. (2010) Polyunsaturated fatty acids, neuroinflammation and well being. *Prostaglandins Leukot. Essent. Fatty Acids* **82**, 295–303
71. Bligh, E. G., and Dyer, W. J. (1959) A rapid method of total lipid extraction and purification. *Can. J. Biochem. Physiol.* **37**, 911–917
72. Molenaar, M. R., Jeucken, A., Wassenaar, T. A., van de Lest, C. H. A., Brouwers, J. F., and Helms, J. B. (2019) LION/web: a web-based ontology enrichment tool for lipidomic data analysis. *Gigascience* **8**, giz061
73. Gao, F., Tom, E., Lieffrig, S. A., Finnemann, S. C., and Skowronska-Krawczyk, D. (2023) A novel quantification method for retinal pigment epithelium phagocytosis using a very-long-chain polyunsaturated fatty acids-based strategy. *Front. Mol. Neurosci.* **16**, 1279457
74. Sakami, S., Kolesnikov, A. V., Kefalov, V. J., and Palczewski, K. (2014) P23H opsin knock-in mice reveal a novel step in retinal rod disc morphogenesis. *Hum. Mol. Genet.* **23**, 1723–1741
75. MacLean, B., Tomazela, D. M., Shulman, N., Chambers, M., Finney, G. L., Frewen, B., *et al.* (2010) Skyline: an open source document editor for creating and analyzing targeted proteomics experiments. *Bioinformatics* **26**, 966–968
76. Perez-Riverol, Y., Bai, J., Bandla, C., Garcia-Seisdedos, D., Hewapathirana, S., Kamatchinathan, S., *et al.* (2022) The PRIDE database resources in 2022: a hub for mass spectrometry-based proteomics evidences. *Nucleic Acids Res.* **50**, D543–D552